Department of Physics
Indian Institute of Technology Madras
Chennai – 600036

CP violation in B decays at Belle II

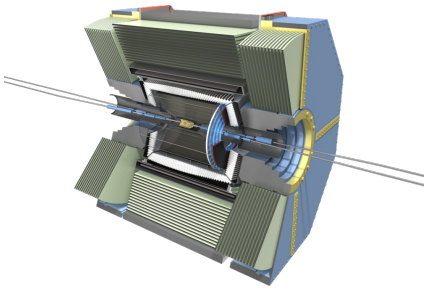

A Thesis

Submitted by

Mehraj Chhetri

For the award of the degree

Of

Master of Science

May 2023

Department of Physics
Indian Institute of Technology Madras
Chennai – 600036

CP violation in B decays at Belle II

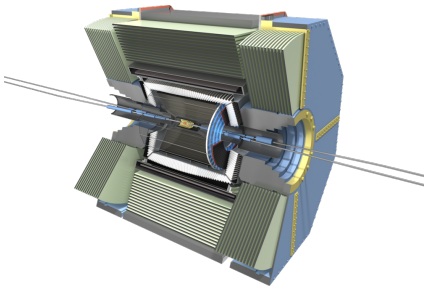

A Thesis

Submitted by

Mehraj Chhetri

For the award of the degree

Of

Master of Science

May 2023

Concern for man and his fate must always form the chief interest of all technical endeavors. Never forget this in the midst of your diagrams and equations.

– Albert Einstein

Acknowledgements

I would like to express my sincere gratitude to my thesis guide, Prof. Jim Libby, for his invaluable guidance, support, and encouragement throughout the course of this project. His depth of knowledge, expertise, and insightful feedback have been instrumental in shaping and refining my work. I am deeply appreciative of his unwavering commitment to my success, which has been demonstrated time and time again through his responsiveness and willingness to help. This thesis would not have been possible without his dedicated supervision, advice and constructive criticisms. I am also grateful for the opportunity he has provided me to work as part of the Belle II collaboration. It has been an honor and a privilege to work with Prof. Jim Libby, and I will always be grateful for his contributions to my academic and professional development.

Abstract

The CP violation in the standard model can be observed through the decay of B meson and a parameter which gives a measure of CP violation is the angle ϕ_3 of the unitarity triangle. Precisely measuring ϕ_3 is an essential test for the standard model, and such measurements can be made using tree-level decays that are unaffected by new physics. The optimal approach for obtaining highly precise measurements of ϕ_3 involves the use of the $B \rightarrow DK$ decay channel, which currently offers the most sensitive method for performing these measurements. This dissertation explores the possibility of measurement of angle ϕ_3 using model-independent Dalitz plot analysis of $B^{\pm} \rightarrow D\,(K^0_L\,\pi^+\pi^-)\,K^{\pm}$ where D can either be D^0 or $\bar{D}^0$. The decay channel is reconstructed using kinematic constraint. The signal is then extracted by employing a fast-boosted decision tree technique to suppress the continuum background. However, the present study concludes that the precision measurement of ϕ_3 cannot be achieved using this mode due to the weak signal strength, which imposes limitations on the statistical accuracy. The analysis is performed on a simulated data sample generated at the $\Upsilon(4S)$ center of mass energy of e^-e^+ collision at Bele II, with an integrated luminosity corresponding to 200 fb^{-1}.

Contents

Page

Acknowledgements **i**

Abstract **iii**

List of Tables **vii**

List of Figures **ix**

Chapter 1 INTRODUCTION **1**

1.1 THE STANDARD MODEL 3
1.2 C, P, AND T SYMMETRIES AND CP VIOLATION 5
1.3 CP VIOLATION IN QUARK SECTOR 8
1.4 DETERMINATION OF UT ANGLE ϕ_3 13
1.4.1 BPGGSZ method to extract ϕ_3 15

Chapter 2 THE BELLE II EXPERIMENT **21**

2.1 THE SUPERKEK ACCELERATOR 21
2.2 THE BELLE II DETECTOR 23
2.2.1 The Vertex detector 25
2.2.2 Central Drift Chamber (CDC) 26
2.2.3 Particle identification system (the ARICH and TOP detector) 27
2.2.4 Electromagnetic Calorimeter (ECL) 31
2.2.5 K_L^0 and muon detector (KLM) 31
2.3 TRIGGER 32

Chapter 3 SELECTION OF $B^\pm \to D(K_L^0\pi^-\pi^+)h$, $h = K/\pi$ EVENTS AT BELLE II **35**

3.1 DATA SAMPLE 35
3.2 EVENT SELECTION 37
3.2.1 Track selection 37
3.2.2 Preselection of K_L^0 candidates 39
3.2.3 Reconstruction of K_L^0 candidates 41
3.2.4 Selection of D candidates 42
3.2.5 Reconstruction of B mesons 44
3.3 CONTINUUM BACKGROUND SUPPRESSION 45
3.3.1 Boosted decision trees (BDT) 47
3.3.2 Variables to suppress continuum events 48
3.3.3 Performance of BDT 51
3.3.4 Figure of merit analysis (FOM) 53
3.4 MULTIPLICITY AND BEST CANDIDATE SELECTION 54

3.5 IDENTIFICATION OF $B^{\pm} \to D^{*}h^{\pm}$ 55

Chapter 4 CONCLUSION AND REMARK 57

Appendix A SIGNAL YIELD DETERMINATION OF $B^{+} \to D(K_L\pi\pi)\pi^{+}$ 59

A.1 MAXIMUM LIKELIHOOD FIT 59
A.2 FIT RESULTS 61
A.2.1 Signal 61
A.2.2 Continuum background 62
A.2.3 Combinatorial background fit 63
A.2.4 Peaking background 64
A.2.5 Combined fit and yield determination 66

Bibliography 69

List of Tables

Table	Caption	Page
3.1	The overall cross-section of different physics processes resulting from collisions at $\sqrt{s}$ = 10.58 GeV	37
3.2	Table of importance of variable	52
A.1	Information of the fit parameter of the ΔE distribution of signal component.	62
A.2	Information of the fit parameter of the ΔE distribution of continuum component.	63
A.3	Information of the fit parameter of the ΔE distribution of combinatorial component.	64
A.4	Information of the fit parameter of the ΔE distribution of peaking component.	65

List of Figures

Figure	Caption	Page
1.1	The standard model of particle physics is divided into fermions (left half) which are the fundamental constituent of matter, and vector and scalar bosons (right half) which are force mediators and gives mass to other SM particles respectively.[1]	4
1.2	Sketch of the unitarity triangle in $\bar{\rho} - \bar{\eta}$	12
1.3	Quark-flow diagram of color-favoured (left) and color-suppressed (right) $B^- \to DK^-$ decay	13
1.4	A schematic representation of the Dalitz plot with kinematic margins. At the boundaries, the momentum of the final state particles is collinear, wherein one particle is going in one direction and the other two are in opposite directions. Inside the plane, the three particles are no longer collinear [2]	17
2.1	Schematic of the superKEKB complex [3, 4]	22
2.2	A schematic of cross-angle and crab crossings	22
2.3	Schematic overview of the Belle II detector [5].	24
2.4	Schematic view of the vertex detector (including PXD and SVD)[6]	25
2.5	dE/dx distribution with respect to momentum of various charged particles in CDC [7]	28
2.6	Schematic view of one of the quartz bars of the TOP counter and internally reflected Cherenkov photons. This image is taken from [8]	29
2.7	A schematic overview of workings of the ARICH detector. The image is taken from [9].	30
2.8	Overview of the Belle II L1 trigger system. Every sub-detector produces an output which goes to the global decision logic (GDL) where the final decision is made. Compared to Belle, the newly added information paths are shown in red. [10]	34
3.1	The distribution of likelihood $\mathcal{L}(K/\pi)$ of charged particle being kaon in signal MC sample	38
3.2	The distribution of prompt hadron's momentum in CM frame in $B^+ \to DK^+$ and $B \to D\pi^+$ signal MC sample	39
3.3	The KLM classifier output distribution. [11]	40
3.4	$\lvert\vec{P}_{K_L} + \vec{P}_{\pi^+} + \vec{P}_{\pi^-}\rvert$ distribution in $B^+ \to D\,(K_L\pi\pi)\,\pi^+$ signal MC sample. The red vertical line shows where the selection is applied.	43
3.5	distribution in $B^+ \to D\,(K_L\pi\pi)\,\pi^+$ signal MC sample. The red dotted line shows where the selection is applied.	43
3.6	M_{bc} distribution of $B^+ \to D\,(K^0_L\pi^+\pi^-)\,K^+$ from signal MC sample (left) and generic MC sample (right). The peak of M_{bc} in signal MC sample is observed at nominal mass of B meson (m_B)	45

3.7 ΔE distribution of $B^+ \to D\ (K^0_L \pi^+ \pi^-)\ K^+$ from signal MC sample (left) and generic MC sample (right). The peak of ΔE in the signal MC sample is observed around 0 45
3.8 Event shape of $e^- e^+ \to q\bar{q}$ (left) and signal (right). The continuum events are produced in a jet-like shape in contrast to $B\bar{B}$ propagating in a spherical shape. Image is taken from [12] 46
3.9 Schematic outline of the decision tree. The x_i, x_j and x_k represent cut variables. Taken from [13] 47
3.10 Top two plot shows the distribution of input variable H^{so}_{02} and H^{so}_{10}. The bottom plot shows the distribution of H^{oo}_2 49
3.11 The distribution of T_{signal} (left) and $|cos\theta^{ROE}_B|$ variable. 50
3.12 The distribution of ΔZ (left) and CLEO Cone 1 (right) is shown. 50
3.13 The plot shows the distribution of variable $|q \cdot r|$ 51
3.14 ROC plot to assess the performance of the BDT. The vertical axis represents the background rejection rate and the horizontal axis is the signal efficiency. The ROC curve for the training and testing set is shown in blue and red colour respectively. 53
3.15 The overtraining plot and the distribution of classifier output. 53
3.16 The optimization of the MVA cut for the BDT trained on $B \to D\pi$ channel. The same cut is obtained for $B \to DK$ 54
3.17 The multiplicity of B candidates after applying all the selection criteria on the channel $B^\pm \to DK^\pm$ in signal MC. The number of multiple candidates event appears to be very few. The distribution before and after the BCS is shown in the right. 55

4.1 The ΔE distribution of different components present in the signal and generic MC. The top plot is for the kaon-enhanced sample $B^+ \to DK^+$ and the bottom plot is for pion enhanced sample $B^+ \to D\pi^+$. The misidentified pions/kaons are represented by magenta. 58

A.1 The ΔE distribution fit of the signal component with the pull distribution. The χ^2/ndof = 1.46 is approximately close to 1 and the pull distribution also is within the ±3 region for the majority of the ΔE range. Thus the crystal ball is a suitable PDF for the above distribution. 62
A.2 The ΔE distribution fit of the continuum component with the pull distribution. The χ^2/ndof = 1.10 is approximately close to 1 and the pull distribution is within the ±3 region for most of the ΔE range. Thus the inverted ARGUS is a suitable PDF for the above distribution. 63
A.3 The ΔE distribution fit of the combinatorial component with the pull distribution. The χ^2/ndof = 1.17 is approximately close to 1 and the pull distribution is within the ±3 region for most of the ΔE range. Thus the crystal ball is a suitable PDF for the above distribution. 64
A.4 The ΔE distribution fit of the peaking component with the pull distribution. The χ^2/ndof = 1.10 is approximately close to 1 and the pull distribution is within the ±3 region for most of the ΔE range. Thus the crystal ball is a suitable PDF for the above distribution. 65

A.5 Final combined fit of the ΔE distribution of $B \to D\pi$ events. The green dashed curve represents the signal component, the red dashed curve represents the continuum components, the black dashed curve represents the combinatorial component and the blue solid line represents the total PDF. 66

Chapter 1

INTRODUCTION

Physics is the study of how things in the universe work. The overarching goal of physics is to understand the behaviour of the universe at all scales, from the largest of galaxy clusters to the smallest of sub-atomic particles. Physicists in order to accomplish this objective, create hypotheses and models to explain physical phenomena, conduct experiments to test and confirm theories, and use measurements and predictions to validate their findings. Particle physicist largely adopts a reductionist perspective. They attempt to explain the universe in terms of the indivisible fundamental entity and its interactions. This idea goes as far back as ancient Greece, where the philosophers at that time pondered over the same thing. One such philosopher was Democritus who argued that if an object is continually broken into smaller pieces, a time will come when it cannot be divided further and he called that entity *atomas* (Greek for "atom"). Now we know that all matter is made up of molecules and molecules are bound states of atoms.

With the advancement in our ability to probe and examine matter with ever-increasing precision, we began to observe matter at smaller and smaller scales. At the beginning of the 20th century, Rutherford (along with Geiger and Marsden) showed that the atom is not indivisible and is made of two components, the electron and the nucleus [1]. It has been discovered that the nucleus consists of neutrons and protons, which in turn are composed of quarks. Therefore, electrons and quarks, to our best understanding, are fundamental.

Another attempt of particle physics is to describe the fundamental forces of nature in

terms of particle mediators. There are four basic fundamental forces, the electromagnetic force, the weak interaction, the strong interaction and the gravitational force. Particle physics successfully explains the first three fundamental forces as particle interactions originated due to the exchange of particle mediators. But it is not yet possible to do so for the gravitational force. Classically, the gravitational field is a manifestation of curvature of space-time by the presence of matter and the quantum mechanical description of the gravitational force is still an unanswered question.

Today, we are aware of 24 fundamental particles and 12 fundamental forces mediator particles. These fundamental particles are

1. 12 quarks: up, down, charm, strange, top and bottom and their corresponding antiparticles

2. 12 leptons: electron, muon, tauon, their corresponding neutrino and their corresponding antiparticles.

3. 12 force mediators : eight gluons, $W^{\pm}$ and Z boson and photon

The model that describes the way these particles behave and interact is called the Standard Model (abbreviated as SM). However, there are still shortcomings of this model as it is unsuccessful in explaining many phenomena. SM does not provide a satisfactory explanation of the observed asymmetry between matter and antimatter in the universe. There is no fundamental particle constituting dark matter and dark energy which makes up almost 95% of the universe. In SM, neutrinos are massless, but recent neutrino oscillation observations in experiments predict that they have mass [14, 15]. SM has been unsuccessful in incorporating the gravitational force (which is encountered most in daily life) into the picture. Due to its inability to explain these and more observations, the Standard Model is considered incomplete, and as a result, there must be a new physics beyond the Standard Model called the New Physics (NP) that can provide a more comprehensive explanation of the universe.

1.1 THE STANDARD MODEL

The standard model is the current best description to describe the fundamental particles and their interaction. The foundation of SM stands on the grounds and principles of Quantum Field Theory, where each particle and their interactions are described in terms of fields. The excitation of these fields gives rise to their respective particle states. These particles' properties are described by the quantum numbers they carry. Spin is an intrinsic quantum number which describes what kind of statistics these particles follow. If the particle spin is half integer then they are called fermions. They have antisymmetric wave function and so they follow Fermi-Dirac statistics. If the particle's spin is integer then they are called a boson. They have symmetric wave function and so they follow Bose-Einstein statistics. All particles in SM are either fermions or bosons. Spin 1/2 fermions in SM are the fundamental particles that makeup all the matter in the universe. Spin 1 bosons are the force-carrying particles and spin 0 boson is what gives masses to all the other elementary particles.

Fermions are classified into quarks (u, d, c, s, t, b) and leptons (e, μ, τ, ν_e, ν_μ, ν_τ). Leptons and quarks can further be grouped into three groups of different generations as shown in 1.1. The second and third-generation fermions resemble the first-generation fermions with consecutively increasing masses. The classification of fermions into quarks and leptons is based on whether they can interact via strong force or not. Quarks can interact strongly so they carry additional quantum numbers along with an electric charge quantum number called color charge. However, leptons cannot interact strongly hence they do not carry color charge and only carry 1 unit of electric charge quantum number. The ability to carry color charge allows quarks to form bound states with each other and create a whole zoo of various particles (hadrons). In fact, free quarks have never been observed, a property called confinement.

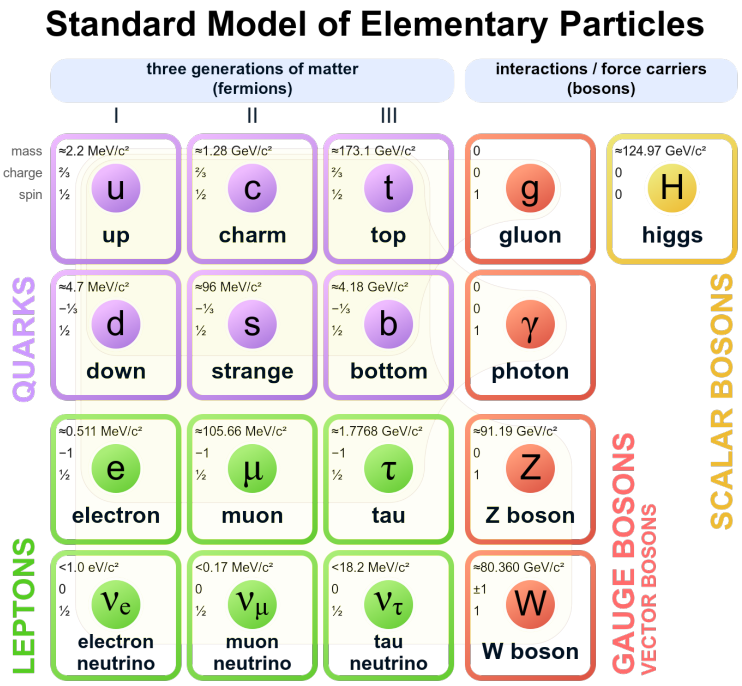

Figure 1.1: The standard model of particle physics is divided into fermions (left half) which are the fundamental constituent of matter, and vector and scalar bosons (right half) which are force mediators and gives mass to other SM particles respectively.[1]

The force mediators in SM are bosons as they carry spin-1. The electromagnetic interaction is mediated via massless spin-1 photon. These are exchanged between particles that carry an electric charge quantum number which also needs to be conserved in this interaction. The electromagnetic force is a long-range force whose strength is larger than weak interaction but it is weaker than strong interaction.

Weak interaction on the other hand is mediated by $W^{\pm}$ and Z^0 which are spin 1 massive bosons. It is the weakest fundamental force in the SM which is the result of the massiveness of the weak bosons. The current associated with Z^0 boson is called neutral weak current and they do not change the flavour of the quark. Whereas the current associated with $W^{\pm}$ bosons are called charged weak current and they change the flavour of the quark. Additionally, the coupling of $W^{\pm}$ with different pairs of quarks is different.

But the $W^{\pm}$ bosons couple equally with all generations of leptons. This is known as the lepton flavour universality.

The mediator of the strong force is called the gluons and they are massless spin 1 bosons. The strong force is short range and the coupling strength of this interaction is stronger than the other two interactions in SM. The gluons carry color charge which is the charge associated with strong interaction (unlike photons which have no charge) as a consequence they can couple with themselves. This is the reason why gluons are the only mediators which participate in the interaction.

With the discovery of the Higgs boson in 2012 [16, 17], the SM model is complete. The Higgs has been a missing puzzle for many centuries until it was discovered. The fermions having mass can interact with. it The Higgs plays the main role in SM of providing mass to the heavy bosons by the process of spontaneous symmetry breaking also known as the Higgs mechanism [18, 19, 20, 21].

The SM model provides us with the ability to make precise predictions of the physical quantities such as lifetime and decay rates, branching fraction of decay and cross-section of various physics processes. Any deviation in the branching fractions and their ratios may hint toward the presence of new physics (NP) in the process.

1.2 C, P, AND T SYMMETRIES AND CP VIOLATION

Symmetry is a very powerful and fundamental concept that plays a very crucial role in physics. Particle physics involves primarily two different types of symmetry - continuous and discrete. These symmetries are associated with the transformation. A continuous transformation is one which can be achieved by a succession of many infinitesimal transformations, as opposed to discrete transformation, which cannot be

achieved in this manner. Continuous transformations result in a gradual, seamless change in the system, unlike discrete transformations which cause an abrupt, sudden change in the system. The dynamical implication of symmetry in these transformations is manifested in Noether's theorem [22] which states that for every symmetry of a physical system, there is a corresponding conserved current which is associated with a conserved charge. For example, if the physical system exhibits transnational and rotational invariance then the conserved quantity associated with them are linear momentum and angular momentum, respectively.

There exist mainly three discrete symmetries in particle physics.

- The charge (C) symmetry states that the fundamental laws of physics remain unchanged when all the particles are substituted with their anti-particles with opposite charges and vice-versa. This leads to a very important conservation law - the conservation of charge. The global version of conservation of charge states that the total charge of an isolated system remains conserved over time. In quantum mechanics, when the charge conjugation operator C is acted on a particle converts it into an antiparticle and all the quantum numbers associated with that of particles such as charge, lepton number, and baryon number also inverts. However, it does not change the chiral nature which is the handedness of the particle. The C symmetry is visible in the strong and electromagnetic interactions as $\hat{C}$ is conserved in these types of processes. However, it is maximally violated in weak interaction [23, 24]. For example, under the operation of $\hat{C}$, the left-handed ν is transformed into left-handed $\bar{\nu}$ which does not exist in SM.

- The parity (P) symmetry is associated with the parity transformation. The parity transformation involves the inversion of the sign of spatial coordinates $(t, x, y, z) \rightarrow (t, -x, -y, -z)$. Stated differently, it reflects the system across a plane of symmetry, giving the impression that the system is being observed through a mirror. Therefore, parity symmetry would imply that the behaviour of the physical system in the mirrored frame should be identical to that in the unmirrored frame. In quantum mechanics, the $\hat{P}$ operator changes the handedness of the particle while keeping the other quantum numbers unchanged. Furthermore, every fermionic particle has an intrinsic parity, which indicated how its wave-function changes under a parity transformation. The fermions have an intrinsic parity of +1 for particles and -1 for anti-particles and they are multiplicative in nature. For example, a meson formed of a quark and an anti-quark will have intrinsic parity of -1. The P is conserved in strong and electromagnetic interaction but it is maximally violated in weak interaction [24]. The P violation of weak interaction is due to

the "$V - A$" (V refers to the vector and A refers to an axial vector) nature of weak current mediated by $W^{\pm}$ bosons.

- The time (T) reversal operation is one which flips the sign of time coordinate $(t, \vec{x}) \rightarrow (-t, \vec{x})$ or the reversal of time direction. The T symmetry would imply that the law of physics should be the same irrelevant of whether the time is running forward or backwards. The T symmetry is believed to hold for strong and electromagnetic interaction but it is violated in the weak interaction [24].

When C and P symmetry were observed to be violated in weak interactions, it was believed that the combination of C and P would be conserved in all interactions. The $\hat{C}\hat{P}$ operator would convert and particle into its anti-particle with handed reversed. Under the operation of $\hat{C}\hat{P}$, the left-handed ν would transform to right-handed $\bar{\nu}$, both of which exist. The CP symmetry was believed to be unbreakable till 1964 when Cronin and Fitch observed the first CP violation in the decay of neutral Kaons [25]. The long-lived neutral Kaons primarily decay to CP odd state which consists of $3 - \pi$, but a very small percentage of K_L^0 were also found to decay into CP even state which consists of $2 - \pi$. This suggested that CP is being violated, but the violation was found to be of a small scale. The CP violation is observed in the decay of several other particles, such as B mesons and D mesons. The Belle, BaBar and LHCb collaborations observed CP violation in B meson decays [26, 27, 28, 29], while the LHCb collaboration has observed CP violation in D^0 decays [30].

There are mainly three types of CP violation

1. Direct CP violation: When the decay rate of particle and its anti-particle are different and the magnitude of the amplitudes of decay of particle (A) and its CP conjugate state $(\bar{A})$ is not equal $\left|A/\bar{A}\right| \neq 1$.

$$\Gamma(A \rightarrow f) \neq \Gamma(\bar{A} \rightarrow \bar{f}) \tag{1.1}$$

   In other words, the violation in the decay can be seen directly.

2. CP violation in mixing: When the two neutral mesons can mix with each other and the mixing rate between two CP conjugates state in the neutral mesons differ.

$$\Gamma(A^0 \rightarrow \bar{A}^0) \neq \Gamma(\bar{A}^0 \rightarrow A^0) \tag{1.2}$$

3. Indirect CP violation : When the neutral mesons and its CP conjugate state decay to the same final state f. Due to the mixing of the neutral meson, there exists an interference of decay amplitudes. The particle A^0 can directly go to f ($A^0 \rightarrow f$) or it can first convert to $\bar{A^0}$ and then decay to f ($A^0 \rightarrow \bar{A}^0 \rightarrow f$). This causes the decay rate of $\Gamma(A^0 \rightarrow f)$ and $\Gamma(\bar{A^0} \rightarrow f)$ to differ as a function of the decay time which cannot be explained by direct CP violation.

However, under the simultaneous operation of charge (C), parity inversion (P) and time reversal (T) operation, the behaviour of all interactions must be invariant. This is the result of the CPT theorem [31], which states that, for a quantum field theory to be Lorentz-invariant and maintain causality, the CPT symmetry must hold. As a consequence of this theorem, the mass and lifetime of a particle and its anti-particle are identical. There have been no experiments which have reported violation of CPT symmetry.

The present universe is matter dominated. This suggests that somewhere in the timeline between the big bang and the present, there has been an asymmetry in matter and antimatter. Andrei Sakharov in 1967 [32], proposed three conditions for the presence of matter-antimatter asymmetry in the early universe,

1. Violation of baryon number
2. C and CP violation
3. Thermal equilibrium

However, the amount of CP violation in SM is too small for the amount of matter domination to be there in the present universe. Hence, physicists are actively searching for new sources of CP violation outside of the SM.

1.3 CP VIOLATION IN QUARK SECTOR

The CP violation in the SM, after its first observation in neutral kaon systems, was introduced by Makoto Kobayashi and Toshihide Maskawa. They build up on the idea of the Cabibbo flavour mixing mechanism [33] and extended this idea to the third generation

of quarks. According to the Cabibbo hypothesis, the weak bosons would couple to weak eigenstates and they are different from mass eigenstates. There is a relation between the weak eigenstate and the mass eigenstate and they are related by a unitary matrix

$$\begin{pmatrix} d' \\ s' \end{pmatrix} = \begin{pmatrix} \cos\theta_c & \sin\theta_c \\ -\sin\theta_c & \cos\theta_c \end{pmatrix} \begin{pmatrix} d \\ s \end{pmatrix}. \tag{1.3}$$

Here θ_c is the Cabbibo angle and it indicates the amount of mixing in the quark. The limitation of the Cabibbo mechanism was that it gave no explanation of the CP violation. For CP violation to be there, there must be a complex phase factor in the Cabbibo unitary matrix so that it can enter into the transition matrix element calculation $\mathcal{M}$ and cause a difference in the transition rate between decay and its CP conjugate. If one attempts to introduce a complex factor manually, it can always be eliminated by rephasing the wavefunction of the d and s quarks. However, If we were to adopt the six-quark model, the 3×3 unitary matrix would have too many phases that cannot be absorbed by the wave function. Employing this idea, Kobayashi and Maskawa introduced the third generation of quarks (top and bottom). By doing so, the CP violating complex phase factor appeared naturally in the 3×3 quark mixing matrix, also known as Cabbibo-Kobayashi-Maskawa (CKM) matrix [34]. The CKM matrix relates the weak and mass eigenstates as

$$\begin{pmatrix} d' \\ s' \\ b' \end{pmatrix} = \begin{pmatrix} V_{ud} & V_{us} & V_{ub} \\ V_{cd} & V_{cs} & V_{cb} \\ V_{td} & V_{ts} & V_{tb} \end{pmatrix} \begin{pmatrix} d \\ s \\ b \end{pmatrix}. \tag{1.4}$$

The CKM matrix is a 3×3 unitary matrix, so it requires 4 parameters to describe the matrix (3 mixing angles and 1 complex phase).

$$V_{CKM} = \begin{pmatrix} 1 & 0 & 0 \\ 0 & c_{23} & s_{23} \\ 0 & -s_{23} & c_{23} \end{pmatrix} \begin{pmatrix} c_{13} & 0 & s_{13}e^{-\iota\delta} \\ 0 & 1 & 0 \\ -s_{13}e^{\iota\delta} & 0 & c_{13} \end{pmatrix} \begin{pmatrix} c_{12} & s_{12} & 0 \\ -s_{12} & c_{12} & 0 \\ 0 & 0 & 1 \end{pmatrix} \tag{1.5}$$

where $s_{ij} = \sin\theta_{ij}$ and $c_{ij} = \cos\theta_{ij}$.

The 3 mixing angles and complex phase are free parameters in the SM along with the masses, charge, and gauge coupling of three symmetries ($U(1)$, $SU(2)$, $SU(3)$) and Higgs potential parameters. These values are constants of nature just like the speed of light and Planck's constant. Therefore, these can only be calculated by empirical means. The experiments only allow us to measure the magnitude of the elements of the CKM matrix and they are determined using the decays of Kaons, D^0 and B^0 [35].

$$|V_{CKM}| = \begin{pmatrix} 0.97383 \pm 0.00024 & 0.2272 \pm 0.0010 & 0.00396 \pm 0.00009 \\ 0.2271 \pm 0.0010 & 0.97296 \pm 0.00024 & 0.04221 \pm 0.00045 \\ 0.00814 \pm 0.00048 & 0.04161 \pm 0.00012 & 0.999100 \pm 0.000034 \end{pmatrix} \quad (1.6)$$

It can be observed empirically that the third generation quarks have little interaction with the other two generations as there is hardly any mixing with the other two ($s_{12} \gg s_{23} \gg s_{13}$).

Another widely used parameterisation of the CKM matrix is the Wolfenstein Parameterisatin [36]. It is used to express the elements of the CKM matrix in powers of λ, where $\lambda = \sin\theta_{12} \approx 0.22$. The 4 real parameters used to describe the CKM matrix are λ, A, ρ and η which are related to the mixing angles and the complex phase as,

$$s_{12} = \lambda, \quad (1.7)$$

$$s_{23} = A\lambda^3, \quad (1.8)$$

$$s_{13}e^{-\iota\delta} = A\lambda^3(\rho - \iota\eta) \quad (1.9)$$

The CKM matrix in this parameterisation, up to 4th power of λ, is given by,

$$V_{CKM} = \begin{pmatrix} 1 - \frac{\lambda^2}{2} & \lambda & A\lambda^3(\rho - \iota\eta) \\ -\lambda & 1 - \frac{\lambda^2}{2} & A\lambda^2 \\ A\lambda^3(1 - \rho - \iota\eta) & -A\lambda^2 & 1 \end{pmatrix} + \mathcal{O}(\lambda^4) \quad (1.10)$$

The CKM matrix parameter η, which makes the element V_{ub} and V_{td} complex, characterizes the phase that violates CP symmetry. In the absence of CP violation in the

Standard Model, this parameter would be zero. This representation of the CKM matrix allows us to approximate the CKM matrix with a desired level of precision by truncating the power series to a specific order in λ.

The CKM matrix can be geometrically visualised in the complex plane using the unitary triangle. The equation that defines the unitary triangle is obtained by using the unitarity condition $VV^{\dagger} = V^{\dagger}V = I$. This condition implies that its rows and columns are orthogonal,

$$\sum_{k=u,c,t} V_{ki}^{*} V_{kj} = \delta_{ij} \tag{1.11}$$

where $k, j \in \{d, s, b\}$. With this condition, it would be possible to obtain six distinct equation that represents six separate triangles in a complex plane having the same area which itself serve as a measure of the degree of CP-violation in SM. The most widely used relation which corresponds to the unitarity triangle is

$$\frac{V_{ub}^{*} V_{ud}}{V_{cb}^{*} V_{cd}^{*}} + 1 + \frac{V_{tb}^{*} V_{td}}{V_{cb}^{*} V_{cd}} = 0 \tag{1.12}$$

This relation is obtained by the inner product of the first and third columns of the CKM matrix which is more important than others because the sides of the triangle are of the same order of magnitude $O(\lambda^3)$. The triangle obtained using the above equation is shown in Fig [1.2].

where the angles of the unitary triangle is given by,

$$\alpha = \phi_2 = \arg\left(-\frac{V_{tb}^{*} V_{td}}{V_{ub}^{*} V_{ud}}\right) \tag{1.13}$$

$$\beta = \phi_3 = \arg\left(-\frac{V_{cb}^{*} V_{cd}}{V_{tb}^{*} V_{td}}\right) \tag{1.14}$$

$$\gamma = \phi_3 = \arg\left(-\frac{V_{ub}^{*} V_{ud}}{V_{cb}^{*} V_{cd}}\right) \tag{1.15}$$

The sides of the triangles indicate the magnitude of the elements of the CKM matrix and the angles of the triangles indicate the complex phases. The CP-violating phase of the

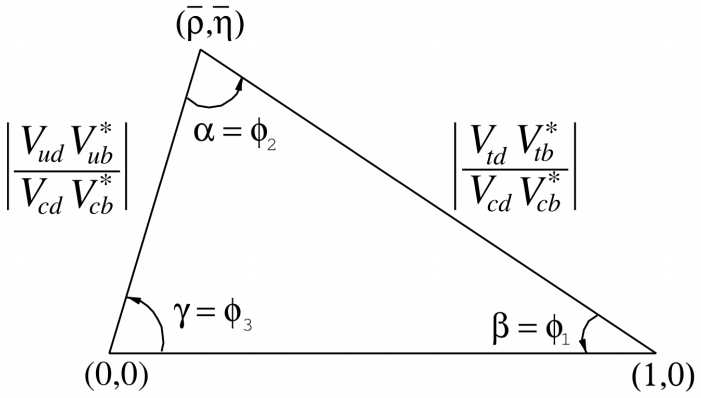

Figure 1.2: Sketch of the unitarity triangle in $\bar{\rho} - \bar{\eta}$

CKM matrix is related to the angle γ and β which describes the mixing of quarks in the weak interaction. If there were no CP-violation, then the angle γ and β would have been zero and the unitarity condition 1.12 would describe a line rather than a triangle.

The experimental measurements of the sides and angle of the unitarity triangle can be done using various decay channels of B meson. The precise measurements of the sides and angles of the triangles provide us with means to test the SM. By measuring the sides and angles in multiple decay channels, it is possible to overconstrain the unitarity triangle, thereby allowing for a more stringent test of the predictions of the Standard Model.

The precision measurement of angle ϕ_3 is substantial because it can be cleanly measured with tree-level decay modes without much theoretical uncertainty [37]. Tree-level processes are typically not significantly impacted by the presence of New Physics (NP) unlike loop-level decays which are more prone to the effects of NP. Hence if angle ϕ_3 is measured with high precision, it can serve as a benchmark for assessing the possible existence of NP by examining its agreement with UT parameters [38]. The present global average value of the direct measurement of the angle ϕ_3 is $(66.2^{+3.4}_{-3.6})^\circ$ [39] and

the value coming from the indirect interpolation is $(65.6^{+0.9}_{-2.5})^\circ$ [40] which is consistent with the SM predictions.

It is not feasible to estimate the angles of the unitarity triangle through experimental measurements of branching fractions, as such measurements can only aid in determining the magnitude of CKM matrix elements on the triangle's sides. In order to probe the angles, measurements must be done on the quantities which are directly sensitive to the transition amplitude rather than the squared amplitude.

1.4 DETERMINATION OF UT ANGLE ϕ_3

To determine the angle ϕ_3, the most effective approach is to make use of the interference between the decay amplitudes of tree-level quark transitions $b \to c\bar{u}s$ and $c \to \bar{c}us$ as these decays do not involve any loop-level diagrams and B mixing. Hence, the theoretical uncertainty becomes almost negligible $\mathcal{O}(10^{-7})$ [41]. The ideal mode to conduct this analysis is through the examination of the decay mode $B^+ \to DK^+$, where D is in a superposition of D^0 and $\bar{D}^0$ decaying to a common CP eigenstate f. The dependence on ϕ_3 arises from the interference between the $B^\pm \to \bar{D}^0 K^\pm$ and $B^\pm \to D^0 K^\pm$.

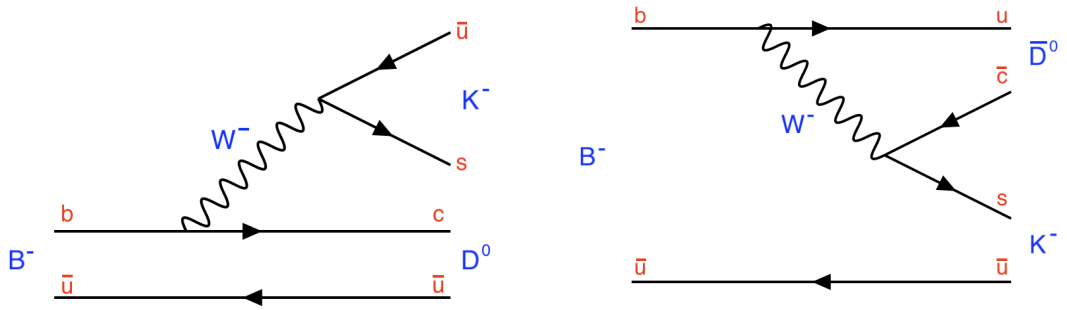

Figure 1.3: Quark-flow diagram of color-favoured (left) and color-suppressed (right) $B^- \to DK^-$ decay

The mode $B^- \to D^0 K^-$ is identified as the color-favoured mode and $B^- \to \bar{D}^0 K^-$ is

identified as color-suppressed, which is also evident from the quark flow diagram Fig. 1.3. In the color-favoured diagram, given the color of the b quark in B^- meson, the quarks of K^- can be in three different color states, but the quark in K^- of the color-suppressed diagram can only carry one color and must be the same as the b quark. Along with the color-suppressed mode, the second decay mode is also CKM-suppressed. If the amplitude of color-favoured mode is $\mathcal{A}(B^- \to D^0 K^-) \equiv A$, then it follows that amplitude of color-suppressed mode is $\mathcal{A}(B^- \to \bar{D}^0 K^-) \equiv A r_B e^{\iota(\delta_B - \phi_3)}$, where δ_B is the strong phase difference, ϕ_3 is weak phase difference, and

$$r_B = \frac{|\mathcal{A}(B^- \to \bar{D}^0 K^-)|}{|\mathcal{A}(B^- \to D^0 K^-)|} = \frac{|V_{ub}||V_{cs}|}{|V_{us}||V_{cb}|} \times \frac{1}{3} \approx 0.1 \tag{1.16}$$

The factor $1/3$ appears due to the color suppression of the second diagram. The decay rate, therefore, is proportional to,

$$\Gamma \propto |\mathcal{A}(B^- \to DK^-)|^2 = |\mathcal{A}(B^- \to D^0 K^-) + \mathcal{A}(B^- \to \bar{D}^0 K^-)|^2 \tag{1.17}$$

$$= A^2 + A^2 r_B^2 + 2A^2 r_B \cos(\delta_B - \phi_3) \tag{1.18}$$

The same can be applied to the amplitude of the CP conjugate state $B^+ \to DK^+$ with a change in the sign of the weak phase ϕ_3. For different final states of the D meson decay, we can utilize the equation 1.17 to estimate different experimental observables which are related to ϕ_3. Depending on the different final states of the D meson, there are different methods of estimating the CP violating observables.

- GLW (Gronau, London and Wyler) method [42]: Utilizes the decay of D meson to states K^+K^-, $\pi^+\pi^-$ or $K^0_S\pi^0$.
- ADS (Atwood, Dunietz and Soni) method [43, 44]: Utilizes the decay of D meson to doubly-Cabbibo-suppressed final states such as $K^+\pi^-$, $K^+\pi^-\pi^0$ or $K^+\pi^-\pi^+\pi^-$.
- BPGGSZ (Bondar, Poluektov, Giri, Grossman, Soffer, and Zupan) method [45, 46]: Utilizes the decay of D meson to multi-body CP eigenstates $K^0_S\pi^+\pi^-$ or $K^0_S K^+K^-$.

Among these methods, the best sensitivity is achieved using the BPGGSZ method because of the considerable branching fraction of $D^0 \to K^0_S\pi^+\pi^-$ [47] and excellent K^0_S reconstruction efficiency at Belle II. Due to the presence of only charged particles in the

final state, the reconstruction efficiency is high and the background level is low compared to the neutral particles. Since the D meson decay involved is a three-body decay, one must perform a Daltiz plot analysis on the data to extract the parameters δ_B, r_B, and ϕ_3.

1.4.1 BPGGSZ method to extract ϕ_3

For this method, we consider the decay mode $B^+ \to [D \to K^0_S h^+ h^-]K^+$ where $h = K/\pi$. The amplitude of this decay mode is given by,

$$A_{B+}(m^2_-, m^2_+) = \bar{A}(m^2_-, m^2_+) + r_B e^{\iota(\delta_B - \phi_3)} A(m^2_-, m^2_+), \tag{1.19}$$

where $\bar{A}$ is the amplitude of $\bar{D}^0 \to f$ decay, A is the amplitude of $\bar{D}^0 \to f$ and (m^2_+, m^2_-) are the invariant masses of $(K^0_S\pi^+, K^0_S\pi^-)$ from D-decay which will act as Dalitz plot variable. Here the final state is $f \equiv K^0_S\pi^+\pi^-$. The probability density in the D-decay phase space is,

$$P_B = |A_B|^2 = |\bar{A} + r_B e^{\iota(\delta_B - \phi_3)} A|^2 \tag{1.20}$$

$$= |\bar{A}|^2 + r^2_B|A|^2 + 2r_B \Re(\bar{A}^* A e^{\iota(\delta_B - \phi_3)}) \tag{1.21}$$

Considering,

$$\bar{A}^* A = |\bar{A}||A| e^{\iota(\delta_D - \delta_{\bar{D}})} = |\bar{A}||A| e^{\iota\Delta\delta_D} \tag{1.22}$$

where δ_D and $\delta_{\bar{D}}$ are strong phases for $D^0 \to f$ and $\bar{D}^0 \to f$ decays respectively. Using 1.22, the last term of 1.21 becomes,

$$2\Re(\bar{A}^* A e^{\iota(\delta_B - \phi_3)}) = |\bar{A}||A|(e^{\iota(\Delta\delta_D + \delta_B + \phi_3)} - e^{-\iota(\Delta\delta_D + \delta_B + \phi_3)}) \tag{1.23}$$

$$= 2|\bar{A}||A|(\cos(\Delta\delta_D + \delta_B + \phi_3)) \tag{1.24}$$

$$= 2|\bar{A}||A|(\cos\Delta\delta_D \cos(\delta_B + \phi_3) - \sin\Delta\delta_D \sin(\delta_B + \phi_3)) \tag{1.25}$$

Substituting this in 1.21,

$$P_B = |\bar{A}|^2 + r_B^2|A|^2 + 2r_B|\bar{A}||A|(\cos\Delta\delta_D\cos(\delta_B+\phi_3) - \sin\Delta\delta_D\sin(\delta_B+\phi_3)) \tag{1.26}$$

$$= |\bar{A}|^2 + r_B^2|A|^2 + 2\sqrt{P\bar{P}}(x_-C - y_-S) \tag{1.27}$$

Here we have redefined the quantities,

$$P(m_-^2, m_+^2) = |A|^2 \tag{1.28}$$

$$\bar{P}(m_-^2, m_+^2) = |\bar{A}|^2 \tag{1.29}$$

$$x_- = r_B\cos(\delta_B - \phi_3) \tag{1.30}$$

$$y_- = r_B\sin(\delta_B - \phi_3) \tag{1.31}$$

$$C(m_-^2, m_+^2) = \cos(\Delta\delta_D) \tag{1.32}$$

$$S(m_-^2, m_+^2) = \sin(\Delta\delta_D) \tag{1.33}$$

The density the CP conjugate mode, $B^- \rightarrow DK^-$ is given by,

$$P_{\bar{B}} = |\bar{A}|^2 + r_B^2|A|^2 + 2\sqrt{P\bar{P}}(x_+C + y_+S) \tag{1.34}$$

where $x_+ = r_B\cos(\delta_B+\phi_3)$ and $y_+ = r_B\sin(\delta_B+\phi_3)$.

The subsequent analyses are done on the Dalitz plane. The decay of D meson is a 3-body process and hence it can be visualised using the Dalitz plot. In a 2-body decay process, the final state is fixed by the knowledge of the initial state. However, this is not so in the case of 3-body decay. The three-body decay has 12 degrees of freedom (three unknown 4 momenta). By utilizing the conservation of 4 momenta and considering the isotropic nature of the decay process for scalar particles, the number of degrees of freedom can be reduced to two, given that the initial mass of the final states is already determined. The commonly employed free parameter is two of the three squared invariant masses of the final state particles, defined by

$$m_{ij} = (p_i + p_j)^2 = m_i^2 + m_j^2 + 2(E_iE_j - \vec{p}_i.\vec{p}_j) \tag{1.35}$$

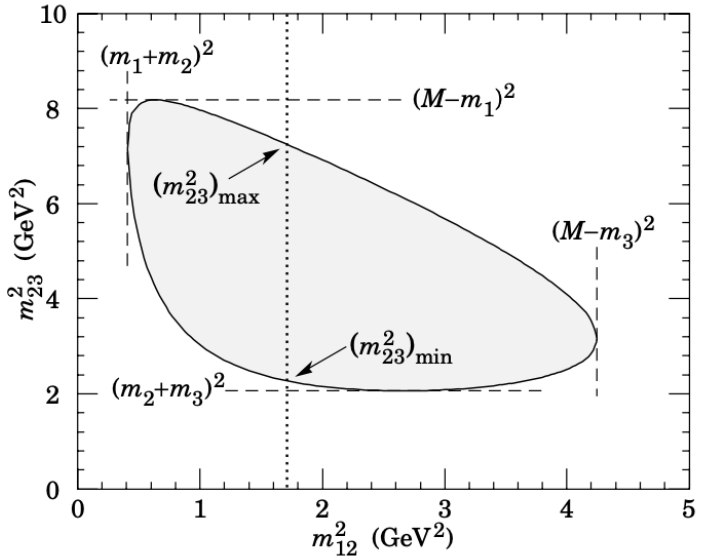

Figure 1.4: A schematic representation of the Dalitz plot with kinematic margins. At the boundaries, the momentum of the final state particles is collinear, wherein one particle is going in one direction and the other two are in opposite directions. Inside the plane, the three particles are no longer collinear [2]

The three invariant masses are related to each other by the relation,

$$m_{12}^2 + m_{23}^2 + m_{13}^2 = M^2 + m_1^2 + m_2^2 + m_3^2 \tag{1.36}$$

where m_1, m_2, m_3 are masses of final state particles and M is the mass of initial particle. The plane of two squared invariant masses is called the Dalitz plane. The Dalitz plot is very convenient for observing the dynamics of the decays. If there are no substructures present then $|\mathcal{M}|^2$ is uniformly distributed throughout the plane. If there are any substructures visible in the plane, then they represent intermediate resonances. One can identify these substructures, which appear as strips, to calculate the mass (M), width (Γ) and spin of the resonance. They also play an important role in studies of the CP violation. CP violation may arise from interference between decays occurring through different resonances and there will be regions in the Dalitz plot where the magnitude of CP violation will be sizeable. We can define binning schemes in the Dalitz plot which isolates the regions in which significant CP violation occurs.

For the estimation of ϕ_3, we need the information on the phase difference between A and $\bar{A}$ at every point in the Dalitz plane. An approach that can be taken is by first constructing a model for $A(m_+^2, m_-^2)$ using the decay $D^{*\pm} \to D\,\pi^\pm$ to tag the flavour of the D meson. The model for A is determined by fitting the amplitude for the flavour sample which is used as an input to fit a $B^\pm \to D^0\,K^\pm$ to obtain r_B, δ_B and ϕ_3. However, this model-dependent approach introduces systematic uncertainty and limits the precision of the measurement of ϕ_3 [[48], [49]].

One can remove the systematic uncertainty by dividing the Dalitz plot into $2N$ bins with bin index running from $i = N$ to $i = -N$ excluding the $i = 0$. The binning layout is symmetric about $m_+^2 = m_-^2$ line and interchanging m_+^2 and m_-^2 is the same as interchanging the bins i and -i. The region corresponding to $m_-^2 > m_+^2$ is labelled by $i > 0$ and the region corresponding to $m_-^2 < m_+^2$ is labelled by $i < 0$. Thus if the point (m_-^2, m_+^2) lies in i'th, then the point m_+^2, m_-^2 will lie in $-i$'th bin. The yield of the flavour-tagged D^0 and $\bar{D}^0$ events in i'th bin region ($\mathcal{D}_i$) of the Dalitz plot is,

$$K_i \propto \int_{\mathcal{D}_i} |A|^2 \mathrm{d}\mathcal{D} \tag{1.37}$$

$$\bar{K}_i \propto \int_{\mathcal{D}_i} |\bar{A}|^2 \mathrm{d}\mathcal{D} \tag{1.38}$$

The K_i and $\bar{K}_i$ can be measured directly from a sample of $D^{*\pm} \to D\,\pi^\pm$ decays and can be used as an input parameter for the analysis of $B^\pm \to D^0 K^\pm$. The yield of $B^+ \to DK^+$ is,

$$N_i^+ \propto \int_{\mathcal{D}_i} |\bar{A}|^2 + r_B^2 |A|^2 + 2|A||\bar{A}|(x_+ \cos\Delta\delta_D - y_- \sin\Delta\delta_D)\mathrm{d}\mathcal{D} \tag{1.39}$$

$$\propto K_{-i} + r_B^2 K_i + 2\sqrt{K_i K_{-i}}(x_+ c_i - y_+ s_i) \tag{1.40}$$

where the quantities c_i and s_i are the i'th bin D-amplitude weighted average of cos and

sin of strong phase difference defined as,

$$c_i = \frac{\int_{\mathcal{D}_i} |A||\bar{A}| \cos(\Delta\delta_D)\mathcal{D}}{\sqrt{\int_{\mathcal{D}_i} |A|^2 \mathrm{d}\mathcal{D}}\sqrt{\int_{\mathcal{D}_i} |\bar{A}|^2 \mathrm{d}\mathcal{D}}} \tag{1.41}$$

$$s_i = \frac{\int_{\mathcal{D}_i} |A||\bar{A}| \sin(\Delta\delta_D)\mathcal{D}}{\sqrt{\int_{\mathcal{D}_i} |A|^2 \mathrm{d}\mathcal{D}}\sqrt{\int_{\mathcal{D}_i} |\bar{A}|^2 \mathrm{d}\mathcal{D}}} \tag{1.42}$$

$$\Delta\delta_D = \delta_D - \delta_{\bar{D}} = \delta(m_-^2, m_+^2) - \delta(m_+^2, m_-^2) \tag{1.43}$$

It can be observed from the above equation that $c_i = c_{-i}$ and $s_i = -s_{-i}$. A similar process can be done for channel $B^- \to DK^-$. Therefore the yield of $B^+(B^-)$ in each bin is,

$$N_i^+ = h_{B^+}(K_{-i} + r_B^2 K_i + 2\sqrt{K_i K_{-i}}(x_+ c_i - y_+ s_i)) \tag{1.44}$$

$$N_{-i}^+ = h_{B^+}(K_i + r_B^2 K_{-i} + 2\sqrt{K_i K_{-i}}(x_+ c_i + y_+ s_i)) \tag{1.45}$$

$$N_i^- = h_{B^-}(K_i + r_B^2 K_{-i} + 2\sqrt{K_i K_{-i}}(x_- c_i + y_- s_i)) \tag{1.46}$$

$$N_{-i}^+ = h_{B^-}(K_{-i} + r_B^2 K_i + 2\sqrt{K_i K_{-i}}(x_- c_i - y_- s_i)) \tag{1.47}$$

where $h_{B^\pm}$ is the normalisation constant and $r_B^2 = x_+^2 + y_+^2 = x_-^2 + y_-^2$. By choosing the number of bins to be $N \geq 3$ (6 observables from B^+ and B^-) and providing c_i, s_i, K_i and K_{-i} as input, it becomes possible to extract $x_\pm$, $y_\pm$ and $h_{B^\pm}$ from single decay mode. After one determines $(x_\pm, y_\pm)$, then it becomes straightforward to estimate r_B, δ_B and ϕ_3.

Charm factories, like BESIII, which collide electrons and positrons at the centre-of-mass energy corresponding to the resonance $\psi(3770)$ $(c\bar{c})$, can be utilized for the measurement of strong-phase parameters (c_i and s_i). In this approach, $D^0\bar{D}^0$ pairs are created in a quantum-correlated state, meaning that the quantum states of the D^0 and $\bar{D}^0$ particles are entangled. As a result, measurements made on one particle can instantaneously determine the quantum state of the other particle. By exploiting this entangled state, the original entangled state of the D^0 and $\bar{D}^0$ pair allows for the determination of the strong-phase parameters without observing the decay of both particles. This method is

more efficient and provides more precise determinations of the strong-phase parameters.

A model-independent BPGGSZ measurement of the angle ϕ_3 using the decay channel $B^{\pm} \rightarrow DK^{\pm}$, where D decays to final state $K^0_S\,\pi^+\,\pi^-$ has already been performed at Belle II [50] and the reported value of ϕ_3 is $(78.4 \pm 11.4 \pm 0.5 \pm 1.0)^\circ$ where the first uncertainty is statistical, the second is experimental systematic uncertainty, and the third is the external systematic uncertainty due to external measurement of c_i and s_i. The focus of this thesis is to investigate the potential feasibility of the decay mode $B^{\pm} \rightarrow D\,(K^0_L\,\pi^+\,\pi^-)\,h^{\pm}$, where $h = \pi/K$, as a means of measuring the angle ϕ_3 at Belle II.

Chapter 2

THE BELLE II EXPERIMENT

This thesis presents an analysis using the simulation data which is produced by considering the design and construction of the Belle II detector. The Belle II detector is part of the High Energy Research Organisation KEK facility in Tsukuba, Japan. It sits at the interaction point of the superKEKB accelerator facility which collides electrons and positrons at the centre of mass energy in the region of $\Upsilon(4S)$ resonance. This chapter gives an overview of the superKEK accelerator, the Belle II detector and its sub-detectors and introduces the reconstruction software framework.

2.1 THE SUPERKEK ACCELERATOR

The superKEK accelerator accelerates the electrons e^- and positrons e^+ to collide them at energies 7 GeV and 4 GeV resulting in the centre-of-mass energy of the collision $\sqrt{s} = \sqrt{4E_{e^-}E_{e^+}} = 10.58$ GeV. The centre-of-mass energy of both particles is enough for the e^- and e^+ to collide and produce $\Upsilon(4S)$ resonance from which many B mesons are produced. Hence it is also called B factory. The e^- and e^+ travel in bunches in the KEK ring facility whose circumference is approximately 3 km. It is an upgrade of the KEK accelerator to increase the instantaneous luminosity by a factor of 40 greater than the peak intensity recorded by KEKB. The important aspects to achieving this are the reduction of beam size by a factor of 20 and an increase in the beam current by a factor of two. This is called the nano-beam scheme and is explained in the next subsection. The schematic view of the superKEKB factory is shown in Fig. 2.1.

The electrons are introduced in the accelerator using an electron injection gun. The electrons are initially accelerated using LINAC before hitting a thick tungsten target

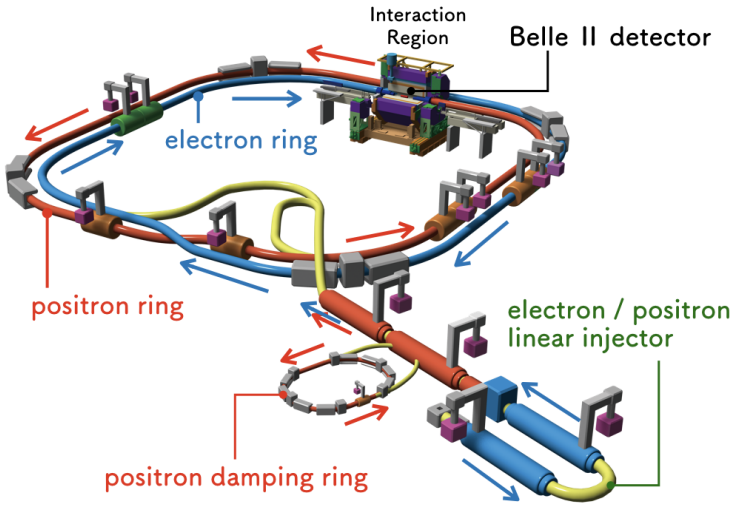

Figure 2.1: Schematic of the superKEKB complex [3, 4]

which produces a shower of particles including positrons. The positrons are then the separated from rest of the shower using a magnetic field. After which, the electrons and positrons enter the storage ring. The electron beam is stored in a high-energy ring (HER) where they are accelerated to energy 7 GeV. Whereas, the positron beam is stored in a low-energy ring (LER) with energy 4 GeV. The two beams are then made to collide at the interaction point at a crossing angle and unique nano-beam scheme where the Belle II detector is placed.

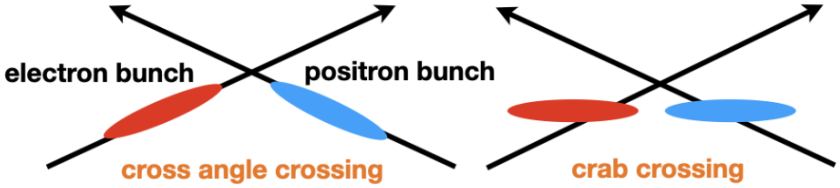

Figure 2.2: A schematic of cross-angle and crab crossings

The beam collides with a crossing angle of ±83 mrad. This ensures that the interaction

region remains clear of any unwanted collisions arising from multiple bunches. It also removes the necessity for any separation-bend magnets, which ultimately help in reducing beam-related backgrounds. To maximize the intensity, two superconducting crab cavities are used to kick the bunches into the horizontal plane so that the collision is head-on. This is illustrated in Fig. 2.2.

2.2 THE BELLE II DETECTOR

The Belle II detector is a general-purpose detector with multiple detector sub-system which surrounds the interaction point of the e^-e^+ collision at superKEKB facility. The detector performs measurements on the particle energy and momenta and also distinguishes the charged particle efficiently. The design of the detector is very similar to its predecessor, the Belle detector, but all its components are either new or substantially upgraded. The detector has excellent vertex resolution and very high track reconstruction efficiency for charged particles. It can perform precise measurements of neutral particle energies and directions and its particle identification system is highly efficient to distinguish pions, kaons, protons, electrons and muons.

The innermost part of the detector consists of the silicon vertex detector (SVD) which accurately determines the decay vertex near the IP and measures the trajectory of a charged particle with good resolution. The central drift chamber (CDC) is the central tracking device which aids the SVD in determining the trajectory of charged particles. The CDC also aids in the identification of charged particles with the dE/dx measurement along with ARICH and TOP counter sub-system. The kaons and pions are produced in abundance at Belle II after the e^- and e^+ collisions and they behave identically at high momentum. The measurements from these three sub-systems are utilized in differentiating the pions and kaons efficiently. The CDC, ARICH and TOP form the particle identification (PID) system. The PID sub-system is surrounded by the

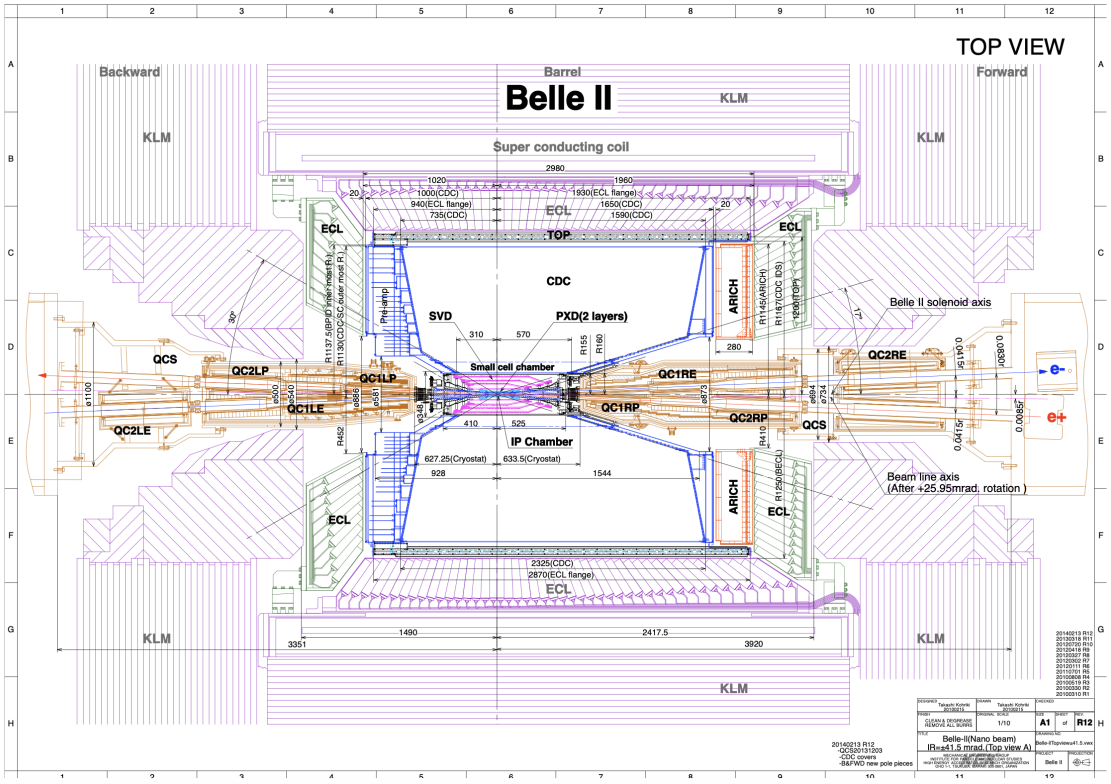

Figure 2.3: Schematic overview of the Belle II detector [5].

crystal calorimeter also called the electromagnetic calorimeter (ECL) which performs the energy deposition measurement of particles that interact primarily via electromagnetic interaction. The whole of the detector is surrounded by a 1.5 T magnetic field superconducting solenoid. The outermost layer of the detector (KLM) measures the long-lived particles that are K_L^0 and muons. The sub-system of the Belle II detector is shown in Fig. 2.3.

The coordinate system that Belle II follows is a right-handed coordinate system with the origin at the IP. The z-axis in the laboratory frame is chosen along the axis of the solenoid with the positive direction along the direction of the electron beam. The positive x-axis is horizontal and points away from the superKEKB ring with the positive y-axis pointing vertically upward. It is more convenient to use a cylindrical coordinate

because of the cylindrically symmetric structure of the detector. The polar angle θ is defined with respect to the positive z-axis and the azimuthal angle ϕ is defined from the positive x-axis.

The subsystem of the Belle II detector is discussed in detail in the upcoming sections.

2.2.1 The Vertex detector

The vertex detector is a semiconductor detector which utilises silicon pixel sensors and silicon strips to detect particles. It comprises six layers in total made of silicon sensors: The first two layers are called the pixel detector (PXD) and the subsequent four layers are called the silicon vertex detector (SVD). Due to increasing beam background levels very close to the IP, the inner layer of the vertex detector is based on pixel sensors instead of silicon stripes. The main purpose of the vertex detector is the reconstruction of the primary and secondary vertex of B, D meson and τ leptons and measure the impact parameter of tracks. The design of the vertex detector is shown in fig 2.4.

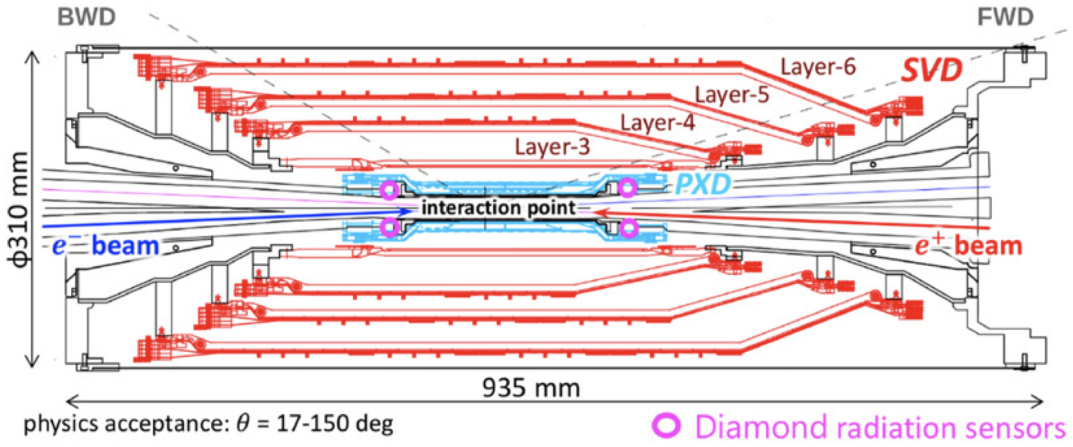

Figure 2.4: Schematic view of the vertex detector (including PXD and SVD)[6]

PXD: The two layers of the PXD are completely made of pixelated sensors with depleted

field effect transistor (DEPFET) technology [51]. One of the benefits of using the DEPFET sensor is that it detects and amplifies the signal itself. In addition, the readout electronics are located outside the acceptance region which helps reduce the material budget by eliminating the need for active cooling inside the detector. The radii of the first and second layers are 14 and 22 mm, respectively and each layer is filled with DEPFET sensors arranged in rectangular modules, known as ladders. The typical size of the pixels in the inner and outer layer is 50×50 μmm^2, respectively 50×75 μmm^2 and each layer is comprised of around 8 million pixels, organized in an array.

SVD: The SVD is formed of four layers of double-sided Si strip detectors with a radius of the remaining four layers to be 38 mm, 80 mm, 115 mm and 140 mm. The angular acceptance region of SVD is $\theta \in [17°,\ 150°]$. The double-sided sensors are configured such that the n and p strips are perpendicular and parallel to the beam direction, respectively. This arrangement allows for the determination of both the x and y coordinates of the hit location. The first SVD layer is composed of small rectangular sensors of thickness 320 μm, while the other three layers are composed of big rectangular sensors of the same thickness and slanted sensors having the trapezoidal form of thickness 300 μm in the forward section. Incorporating a slanted sensor improves the angular acceptance and accuracy of forward-boosted particles. The SVD is capable of performing standalone measurements of low momentum particles that do not reach the CDC, such as pions from K_S^0 decays or soft pions from D^* decays.

2.2.2 Central Drift Chamber (CDC)

The CDC is a multi-wire proportional drift chamber which surrounds two inner semiconductor tracking detectors. It is the central tracking device of the Belle II detector with a large volume drift chamber and small drift cells. The inner cylinder radius is 160 mm and the outer cylinder radius is 1130 mm measured from IP. The CDC overall consists of nine super-layers alternating between axial and stereo layers, with each

super-layer having multiple layers of wires which makes 56 layers in total. The wires in axial layers are aligned parallel to the z-axis and in stereo are slightly tilted with respect to the z-axis to allow for three-dimensional track reconstruction. These layers are immersed in a gas mixture composed of 50% He and 50% C_2H_6, to avoid multiple scattering. The C_2H_6 is utilized to quench the photons generated from electron avalanche and prevent them from scattering and degrading spatial and temporal resolution. The angular acceptance region of CDC is $\theta \in [17°, 150°]$.

The CDC is capable of precisely reconstructing the tracks of charged particles and measuring their momentum. Additionally, it offers particle identification (PID) information by using energy loss (dE/dx) measurements within its gas volume. Moreover, it also provides efficient and reliable 2D and 3D trigger signals for charged particles. When a charged particle passes through the gas chambers, it ionizes the gas and the ions move to nearby sense wires. A tracking algorithm allows the CDC to reconstruct the trajectory of charged particles from the hits in the CDC. By analysing the pulse height and drift time of the ionisation the at anode wire, mean energy deposition (dE/dx) and distance of the particle from the sense wire can be estimated. The dE/dx distribution with respect to momentum in the CDC can be used for particle identification. The separation between different particles is evident in Fig. 2.5 at low momentum values which can be used for PID information.

2.2.3 Particle identification system (the ARICH and TOP detector)

The particle identification (PID) system of Belle II is primarily the Time-of-propagation (TOP) counter and Aerogel Ring-Imaging Cherenkov (ARICH) counter. Both of these detectors utilize the Cherenkov photons produced by relativistic charged particles traversing the radiator material but the operating principles are different. The position of the particle and time of propagation details are provided by the TOP counter and ARICH analyses different ring images for different particles. The information from the

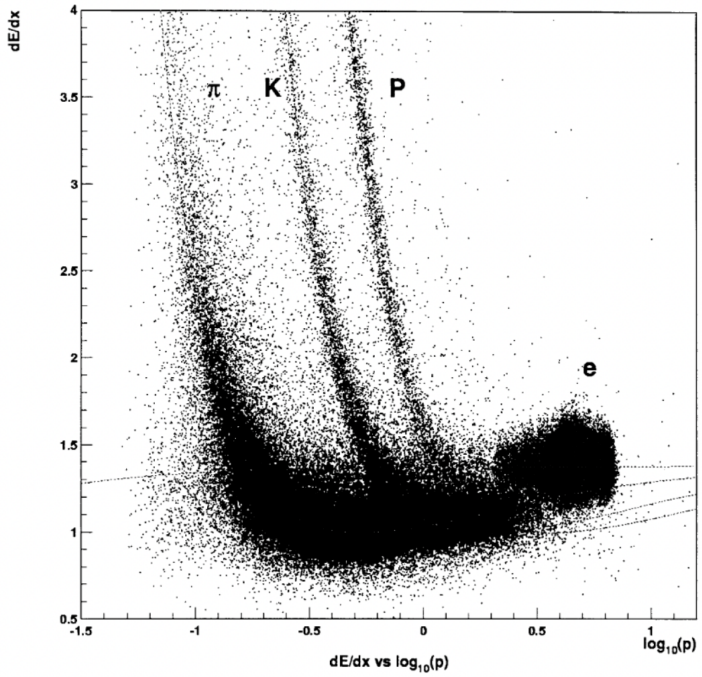

Figure 2.5: dE/dx distribution with respect to momentum of various charged particles in CDC [7]

PID detectors along with momentum measurements by tracking devices and the energy deposit measured by the CDC are combined to determine the mass of the particle.

Time-of-propagation (TOP) counter

The TOP counter is located in the barrel region of the spectrometer, sandwiched between the ECL inner support and CDC outer cover. It estimates the time of propagation of the Cherenkov photon internally reflected in the quartz bar. The main purpose of the TOP counter is to provide identification information of hadrons (mainly π's and K's) having momentum > 1.5 GeV$/c$ where the energy loss information is not discriminated enough by CDC. It is composed of 16 long quartz radiators of thickness 2 cm with readout micro-channel plate photo-multipliers (MCP-PMT) attached on one end of the bar and a spherical focusing mirror attached to the other to focus and direct the Cherenkov photons towards the PMTs. MCP-PMT measure's the time of propagation t_{TOP} of Cherenkov photons. The acceptance region of the TOP counter is $\theta \in [31°, 128°]$. The TOP counter

is illustrated in 2.6

The PID information can be gathered by comparing the time of propagation t_{TOP}

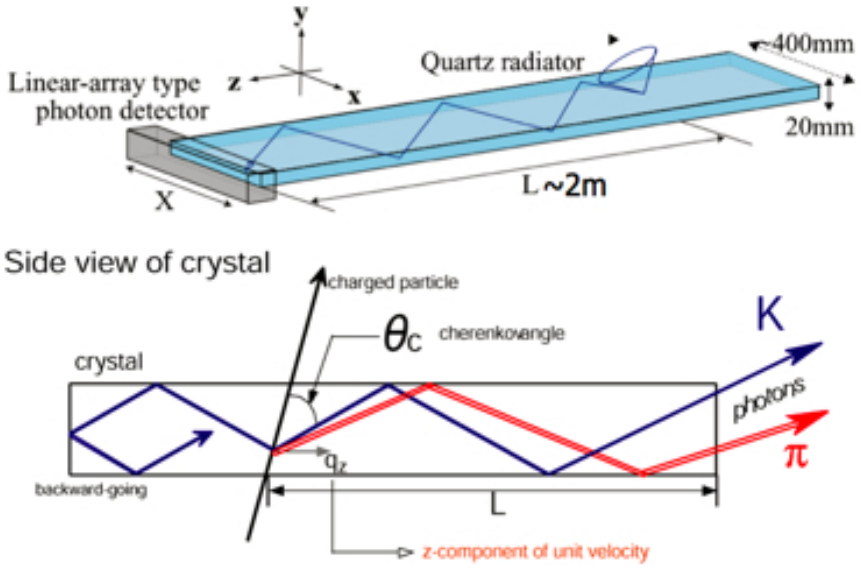

Figure 2.6: Schematic view of one of the quartz bars of the TOP counter and internally reflected Cherenkov photons. This image is taken from [8]

distribution of photons arriving at each MCP-PMT channel with expected PDFs for six standard particles (e^-, μ, π, K, p, d) hypothesis. The expected PDFs have been constructed analytically by providing the mass hypothesis and track parameters [52]. The identification probabilities are then assigned based on the ratio of six corresponding likelihood values.

Aerogel ring imaging Cherenkov (ARICH) counter

Aerogel ring imaging Cherenkov detector (ARICH) is the other PID subsystem which is installed at the forward end-cap and it provides information to distinguish between different particles based on the ring image technique by detecting Cherenkov photons. The ARICH is capable of differentiating between πs and Ks over most of their momentum range. The ARICH detector is illustrated in Fig. 2.7.

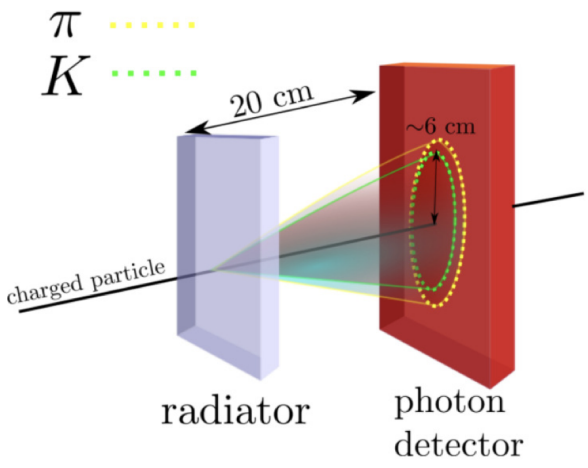

Figure 2.7: A schematic overview of workings of the ARICH detector. The image is taken from [9].

The ARICH is specifically installed in the forward region because the directionality of most events is along the positive z-axis due to the boost. The design of the ARICH detector consists of an aerogel tile with a spacing of 20 cm between the tiles which will allow the ring image of the Cherenkov photon to expand and form on the position-sensitive photon detector also called a hybrid avalanche photon detector (HAPD). As the charged particle passes through the aerogel radiator, it will emit a Cherenkov photon ring which will then be detected by HAPD.

The aerogel radiator is a 2 cm thick layer of silica aerogel with different refractive indices ($n = 1.045$ and $n = 1.055$). It is non-homogenous to increase the yield (N) of Cherenkov photons without degrading the Cherenkov photon angle resolution σ. The performance of the detector is given by the quantity $\sigma/\sqrt{N}$. The two generated Cherenkov rings are then overlapped on the detector surface. The angular acceptance region of ARICH is $\theta \in [14°, 13°]$.

2.2.4 Electromagnetic Calorimeter (ECL)

The crucial role of the ECL is to detect photons with high efficiency and measure the energy of the photon with high precision. In addition to this, it is also used for the identification of electrons and positrons, both online and offline luminosity measurement and the generation of a high-efficiency trigger signal.

When an electron or photon enters the calorimeter made of a crystal absorber, it loses all its energy through bremsstrahlung photons and e^-e^+ pair creation which results in the creation of an electromagnetic shower. The longitudinal propagation of this shower occurs over a characteristic scale that corresponds to the radiation length of the absorber. The energy measurement of the shower along with the information from tracking detectors will help in identifying whether the particle is $e^\pm$ or a photon. In the absence of a charged track leading to the cluster, it can be considered a candidate for a photon, otherwise, it could be an electron or a positron.

The ECL repurposes CsI(Tl) scintillation crystal material from Belle due to its high performance. The ECL covers the barrel, forward end-cap and backward end-cap regions and has an angular acceptance from $\theta \in [17°, 150°]$. There are a total of 8736 crystals with the ends of each crystal glued with a silicon photodiode along with a preamplifier to sense the scintillation light coming from the electromagnetic showers.

2.2.5 K_L^0 and muon detector (KLM)

The KLM detector is the outermost detector designed to detect long-lived particles, mainly K_L^0 and μ^-, which travel a considerable distance within the detector volume and ultimately reach the outermost part. The design of the KLM is composed of alternating layers of iron plates with a thickness of 4.7 cm and a glass electrode resistive plate chamber (RPC) located outside the superconducting solenoid in the barrel region. The

function of the iron plates is to act as a magnetic flux return path for the solenoid. The end-cap region and inner two layers of the barrel are composed of scintillator strips coupled with a silicon photomultiplier (SiPM). Such configuration is required because of the degradation of RPC efficiency due to the high background rate in end-caps and the initial layers of barrel KLM. The angular acceptance of KLM is $\theta \in [20^o, 155^o]$.

For hadrons passing orthogonally through the detector planes, the iron plates contribute an interaction length of 3.9, in addition to the 0.8 interaction length provided by ECL. The RPC and scintillator strips detect the charged particles in the barrel and endcap regions of KLM, respectively. In this thesis, the identification of K_L^0 particles detected exclusively by KLM is crucial. The reconstruction of these particles is challenging due to the significant fluctuations in the development of hadronic showers. As a result, it is possible to determine the direction of K_L^0 but not its energy.

2.3 TRIGGER

The Belle II trigger system identifies interesting events and rejects enormous background events caused by intra-beam scattering and Bhabha scattering. The Belle II trigger system consists of a hardware-based Level 1 trigger (L1) and a software-based High-Level Trigger (HLT). The primary objective of designing these trigger systems is to achieve high efficiency for detecting hadronic events from $\Upsilon(4S) \rightarrow B\bar{B}$ and continuum processes.

In Belle II, the trigger system is comprised of sub-triggers that gather trigger information from sub-detectors. This information is then sent to a global decision logic that makes the final decision regarding triggering. The sub-trigger system plays a crucial role in this process by collecting and transmitting relevant information to the global decision logic. In contrast to HLT, whose primary function is to reject physically uninteresting decays in

real-time, mainly to address storage-related issues. It discards all those events which do not fulfil its selections. This allows for efficient sorting and storage of relevant data for further analysis.

The CDC sub-trigger is capable of providing 2D and 3D tracking information. Neutral and charged-based physics events are provided by the ECL-based triggers, while precise timing and hit topology information is furnished by the Barrel-PID and end-cap PID. The KLM sub-trigger provides muon track information. Upon receiving all the sub-trigger information, the Global Decision Logic (GDL) processes the data and makes the final decision. The right decision is then transmitted as a trigger signal.

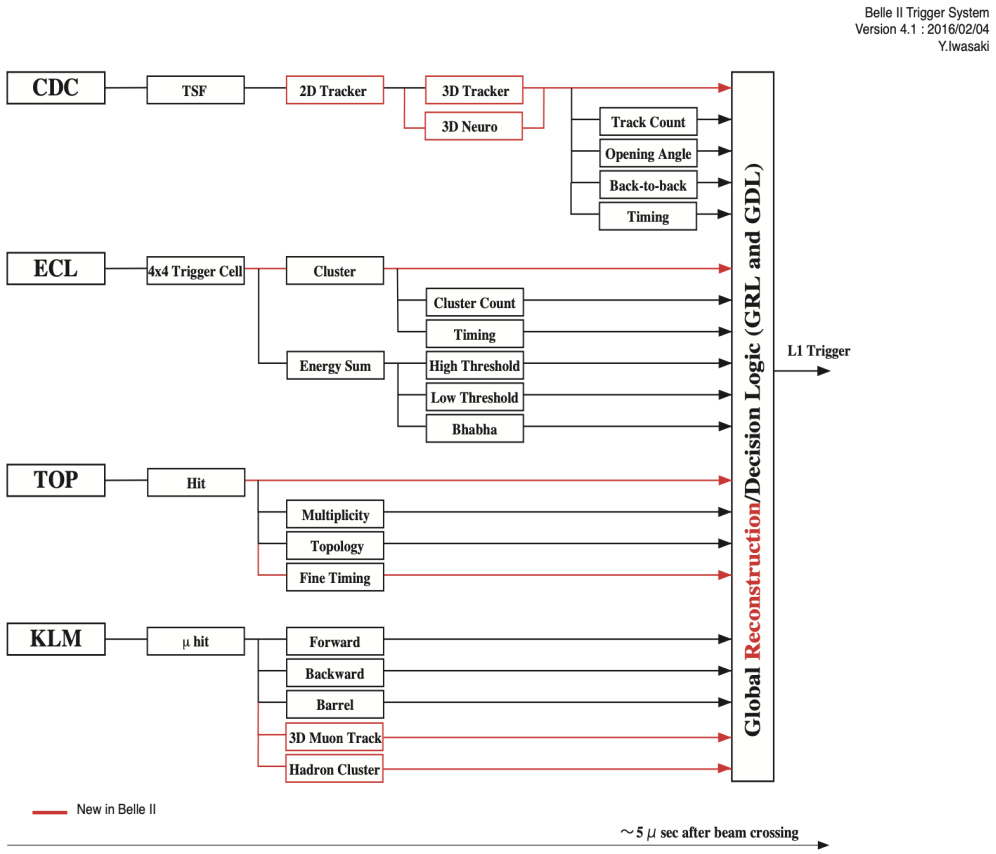

Figure 2.8: Overview of the Belle II L1 trigger system. Every sub-detector produces an output which goes to the global decision logic (GDL) where the final decision is made. Compared to Belle, the newly added information paths are shown in red. [10]

Chapter 3

SELECTION OF $B^{\pm} \to D(K^0_L\pi^-\pi^+)h$, $h = K/\pi$ EVENTS AT BELLE II

This chapter discusses the reconstruction of $B^{\pm} \to DK^{\pm}$ and $B^{\pm} \to D\pi^{\pm}$, where the D meson decays to the final $K^0_L\pi^+\pi^-$. The analysis of both these channels is required to be carried out simultaneously in the context of the model-independent BPGGSZ measurement of CKM angle ϕ_3. This measurement was previously introduced in Chapter 1. The signal mode of interest for this analysis is $B^+ \to DK^+$ due to its high sensitivity to the angle ϕ_3. On the other hand, the channel $B^+ \to D\pi^+$, due to its identical topological structure with the decay $B^+ \to DK^+$ and negligible expected CP violation, acts as a good calibration sample for the signal extraction procedure, if common selections are applied. Furthermore, their simultaneous analysis enables the direct extraction of the $K - \pi$ misidentified background from the data. Because of the Cabbibo-favoured nature of the decay $B^+ \to D\pi^+$, its branching fraction is an order of magnitude larger than that of $B^+ \to DK^+$ decays [47].

The remaining part of this Chapter is organised as follows: the data sample used for the analysis is described in section 3.1. The event selection and K^0_L reconstruction in Belle II is discussed in section 3.2. The background minimization analysis and the procedure are explained in section 3.3. Finally, the best candidate selection and the resulting signal after extraction is discussed in 3.4.

3.1 DATA SAMPLE

The Monte Carlo simulation data for the analysis in this thesis is collected at e^-e^+ center of mass energy $\sqrt{s} = 10.58$ GeV which corresponds to the $\Upsilon(4S)$ resonance. The dataset

consists of signal Monte Carlo (signal MC) data which includes the 1 million sample of each $B^{\pm} \rightarrow D(K^0_L\pi^-\pi^+)K^{\pm}$ and $B^{\pm} \rightarrow D(K^0_L\pi^-\pi^+)\pi^{\pm}$ events corresponding to an integrated luminosity of 173 ab^{-1} and 13.5 ab^{-1} respectively with early phase III detector configuration for the study of the signal events. In addition, generic Monte Carlo sample data corresponding to an integrated luminosity of 200 fb^{-1} is utilised to study the background events. The generic MC data various physics processes after e^-e^+ collision at $\sqrt{s}$ = 10.58 GeV along with their cross-section is shown in Table 3.1.

The simulation data behave as closely as the real-time detector events. These datasets are generated using event generators that simulate the physics process and later, a detailed simulation of the detector is done. By utilizing the simulation data, we can enhance the selection criteria, make the estimation of the efficiency of the signal, train a multivariate discriminant model, identify different components of the backgrounds, and establish a data-fitting model. The simulation of Belle II conitnuum events ($e^-e^+ \rightarrow q\bar{q}$) is produced using KKMC [53] generator interfaced with PYTHIA [54]. The simulation of signal events and $e^+e^- \rightarrow \Upsilon(4S) \rightarrow B\bar{B}$ is generated using EVTGEN software [55]. The Belle II detector simulations were done using GEANT4 [56]. The simulation data samples include the Belle II detector response to the physics processes such as beam-induced backgrounds which includes Touschek scattering due to nano-beam scheme, beam-gas scattering (scattering of beam particle due to residual gas particle in the beam pipe), synchrotron radiation and radiative Bhabha scattering as well as two-photon processes (low momentum e^-e^+ produced via two-photon $ee \rightarrow eeee$) [57]

The final state particles leave measurable signals in the Belle II detector. Stable and long-lived particles, like K^0_L, are detected by various subsystems as described in Chapter 2. Finally, D and B mesons candidates are reconstructed from these final state particles using series C++ algorithms implemented using Belle II Analysis Software Framework

Physics process	cross-section (nb)
$ee \rightarrow \Upsilon(4S)$	1.11
$ee \rightarrow u\bar{u}$	1.61
$ee \rightarrow d\bar{d}$	0.40
$ee \rightarrow s\bar{s}$	0.38
$ee \rightarrow c\bar{c}$	1.30

Table 3.1: The overall cross-section of different physics processes resulting from collisions at $\sqrt{s}$ = 10.58 GeV

(basf2) [58].

3.2 EVENT SELECTION

The generic and signal MC samples are both associated with the official MC production campaigns which are executed using the most recent software version, detector geometry and beam background condition. The description of the generic MC and signal MC sample used in this analysis is discussed in Section 3.1.

This section describes the reconstruction of the decay mode $B^+ \rightarrow D\ (K_L^0\pi^+\pi^-)h^+$.The chain of reconstruction of B meson is,

$$e^+e^- \rightarrow \Upsilon(4S) \rightarrow B^+B^-; \quad B^\pm \rightarrow \bar{D}^0/D^0\ h^\pm; \quad D^0/\bar{D}^0 \rightarrow K_L^0\ \pi^+\ \pi^- \tag{3.1}$$

The D meson candidate can be reconstructed from the three daughter particle K_L^0, π^+ and π^-. The K_L^0 leave a measurable signal in the ECL and KLM subsystems. For the analysis, K_L^0 are exclusively selected from the KLM clusters.

3.2.1 Track selection

In order to ensure that the charged particles K^+ and π^+ in the decay 3.1 originate solely from e^+e^- collisions, the charged track must originate within 0.2 cm radially and 1 cm along the z direction. This eliminates those tracks that arise from the beam-induced background and material interactions. An additional selection $\cos\theta \geq -0.6$ is employed

on the prompt hadrons i.e. π/K coming from the decay of B which ensures that the tracks lie within the ARICH and TOP angular acceptance region. This is done so to reduce the $K - \pi$ misidentification rate. The low momentum charged tracks can be easily differentiated using CDC. The information from CDC, TOP and ARICH sub-systems helps in determining whether these tracks belong to either π or K. The PID detectors assign a likelihood value to π and K candidates associated with a charged track. The ratio,

$$\mathcal{L}(K/\pi) = \frac{\mathcal{L}(K)}{\mathcal{L}(K) + \mathcal{L}(\pi)} \tag{3.2}$$

is used to identify π or K candidates. The selection criteria $\mathcal{L}(K/\pi) > 0.6$ is employed to separate the kaons and pions originating directly from the $B^{\pm} \longrightarrow D\ h^{\pm}$ decays. The kaon-identification efficiency and pion-misidentification rate in Belle II data is 79% and 7% respectively. The distribution of $\mathcal{L}(K/\pi)$ is shown in figure 3.1.

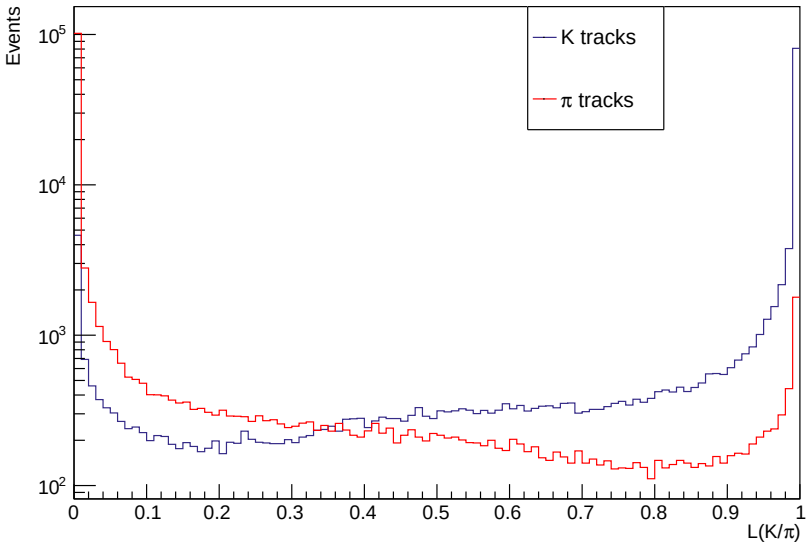

Figure 3.1: The distribution of likelihood $\mathcal{L}(K/\pi)$ of charged particle being kaon in signal MC sample

In addition, based on the signal MC data, it appears that a significant number of the

highest momentum hadrons (prompt hadrons) (K/π) which are exclusively arising from decay $B^{\pm} \rightarrow Dh^{\pm}$ are clustered in a narrow range of the center of mass momentum distribution. This suggests that it is possible to apply selection criteria within the range of $2.1 \leq P_{CMS} \leq 2.5$ without significantly reducing the number of signal events.

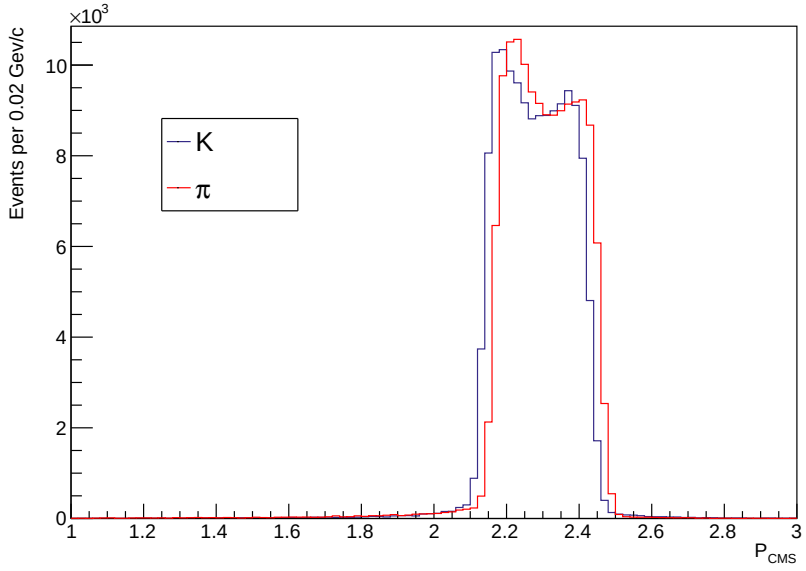

Figure 3.2: The distribution of prompt hadron's momentum in CM frame in $B^+ \rightarrow DK^+$ and $B \rightarrow D\pi^+$ signal MC sample

3.2.2 Preselection of K_L^0 candidates

The detection of K_L^0 can be achieved by observing its interaction with the KLM sub-detector. However, other neutral hadrons coming from $\Upsilon(4S)$ and beam-background also produce hadronic shower in KLM. The dominant source of background stems from neutrons and photons resulting from the interaction of the beam with the detector or beam-pipe material, followed by neutral particles originating from the primary interaction.

To distinguish clusters generated by K_L^0 from those produced by other hadrons, a multivariate analysis is performed at Belle II through the use of a stochastically gradient-boosted decision tree (BDT) to build classifiers. The classifiers are trained on a K_L^0 originating from the $\Upsilon(4S)$. The classifier utilises variables such as cluster shapes, kinematic variables, and information from other detectors and algorithms to produce

a classifier ID which determines the true K_L^0 cluster. The variable with the highest importance are,

- Distance to the next track: the tracks are expected to be consistent with neutral hadrons, i.e. there must be no track leading to the cluster.
- Cluster timing: clusters produced by hadrons arising from beam background are likely to be out of sync with the primary collision.
- Number of inner-most layer hit: the radius of hadronic clusters is expected to be wider than that of electromagnetic clusters.

The distribution of this classifier ID is shown in figure 3.3. The efficiency and background rejection rate was compared for two K_L-id cut values, 0.05 and 0.2. It was shown that while the efficiency at 0.05 is higher than at 0.2, the background rejection rate of the later is higher than the former, [11]. For the subsequent analysis, the K_L-ID threshold is set to 0.25 to further improve the signal-to-background ratio. In addition, to help remove any spurious clusters, the number of KLM cluster layers $N_{layer} \geq 2$.

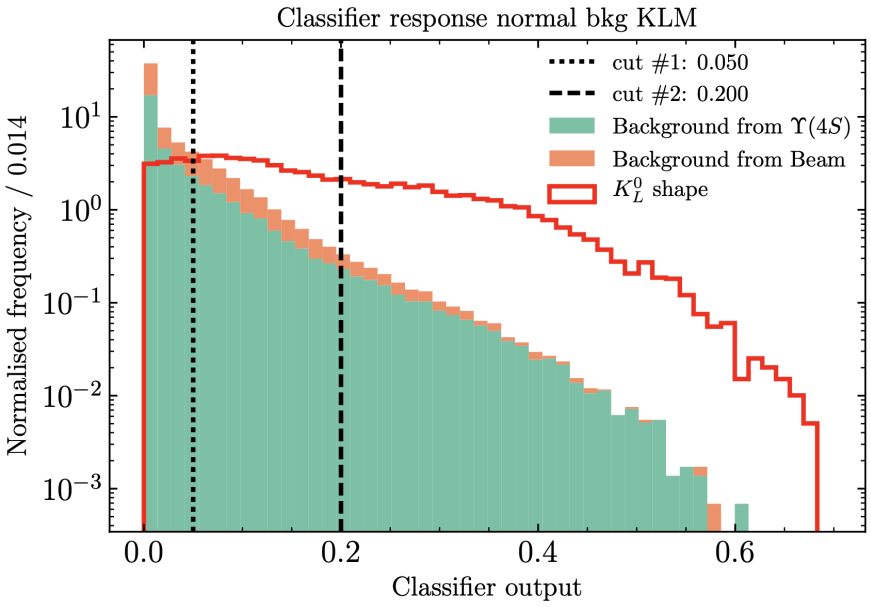

Figure 3.3: The KLM classifier output distribution. [11]

The energy deposition mechanism of KLM does not yield an accurate measurement of the four-momentum of the K_L^0 particles. However, the location of the KLM cluster can

be known accurately which can be used to construct the K_L^0 four-momentum by applying kinematic constraint and fixing the B meson mass. This analysis is explained in the next subsection.

3.2.3 Reconstruction of K_L^0 candidates

The K_L^0 momentum can be reconstructed by requiring momentum conservation and constraining the B mass in the $B^+ \to D\ (K_L^0\pi^+\pi^-)\ h^+$ decay. The momentum of π and h are known as they are track-based particles. The events are first partially reconstructed using the basf2 framework, after which kinematic constraint is applied in ROOT to construct K_L.

The four-momentum of K_L^0 can be written as,

$$P^{\mu}_{K_L} = (E_{K_L}, \vec{P_{K_L}}) = (\sqrt{|\vec{P}_{K_L}|^2 + m^2_{K_L}},\ |\vec{P}_{K_L}|\hat{n}) \tag{3.3}$$

where $\hat{n}$ is the location of the cluster in the center-of-mass frame and is given by $\hat{n} = (\sin\theta\cos\phi, \sin\theta\sin\phi, \cos\theta)$ (polar angle θ and azimuthal angle ϕ in Belle II coordinate system).

Applying 4-momentum conservation,

$$P_B = P_D + P_h \tag{3.4}$$

$$P_B = P_{K_L} + (P_{\pi^-} + P_{\pi^-} + P_h) \tag{3.5}$$

$$P_B = P_{K_L} + P_{\pi\pi h} \tag{3.6}$$

Here $P_{\pi\pi h} = P_{\pi^-} + P_{\pi^-} + P_h$. By squaring both side and fixing the mass of B meson to its PDG value $m_B = 5.279$ [47],

$$m_B^2 = m_{K_L^2} + m^2_{\pi\pi h} + 2(E_{\pi\pi h}E_{K_L} - \vec{P_{\pi\pi h}} \cdot \hat{n}|\vec{P_{K_L}}|) \tag{3.7}$$

$$(E^2_{\pi\pi h} - t^2)|\vec{P}_{K_L}|^2 - 2M^2 t|\vec{P}_{K_L}| + (E^2_{\pi\pi h}m^2_{K_L} - M^4) = 0 \tag{3.8}$$

where the quantities are defined as,

$$M^2 = \frac{m_B^2 - m_{\pi\pi h}^2 - m_{K_L}^2}{2} \tag{3.9}$$

$$t = \vec{P}_{\pi\pi h} \cdot \hat{n} \tag{3.10}$$

Equation 3.7 is a quadratic equation, so in general, P_{K_L} can have two solutions. If both the solutions are kinematically allowed, the one closer to nominal B momentum in center-of-mass is used for further analysis.

3.2.4 Selection of D candidates

The D meson is reconstructed from pair of oppositely charged pions track and K_L^0 candidate. After applying the kinematic constraint and reconstructing K_L^0, the D meson momentum can be determined as,

$$P_D = P_{K_L} + P_{\pi^+} + P_{\pi^-} \tag{3.11}$$

The distribution of the momentum magnitude of the D meson in the center-of-mass frame displays an interesting characteristic where the majority of $|\vec{P_D}|$ seems to be concentrated within a limited range. A selection is applied to $|\vec{P_D}|$ to restrict its value to range $(2.0, 2.6)$ GeV/c.

The distribution of the invariant mass of the daughter of D meson is shown in Figure 3.5. The root-mean-square of the $M_{K_L\pi\pi}$ is found to be $\sigma = 0.0694$. It is required that the invariant mass of the daughter particle be in the range $(2.077, 1.657)$ GeV/c^2 which corresponds to $\pm 3\sigma$ with the nominal mass of D meson (see [47]) lying in this range.

The invariant mass of $\pi^+\pi^-$ originating from the three-body decay $D \rightarrow K_L^0\, \pi^+\, \pi^-$ is

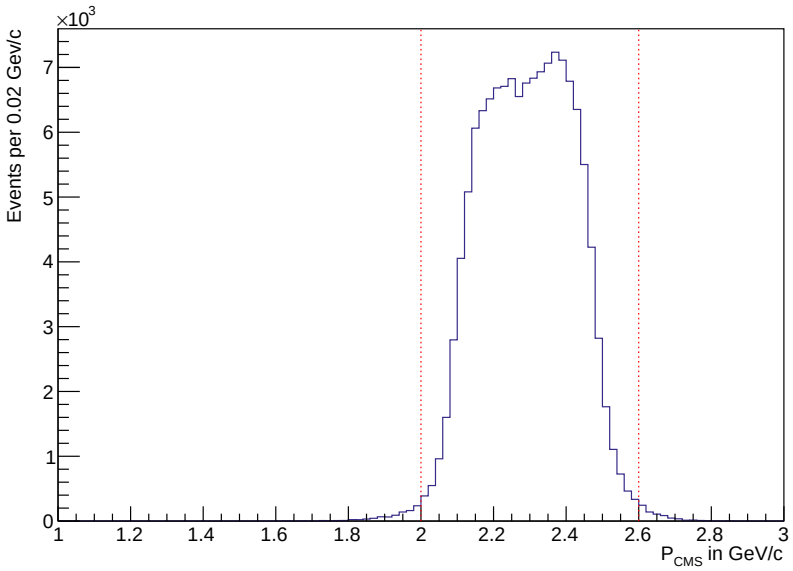

Figure 3.4: $|\vec{P}_{K_L} + \vec{P}_{\pi^+} + \vec{P}_{\pi^-}|$ distribution in $B^+ \to D\ (K_L\pi\pi)\ \pi^+$ signal MC sample. The red vertical line shows where the selection is applied.

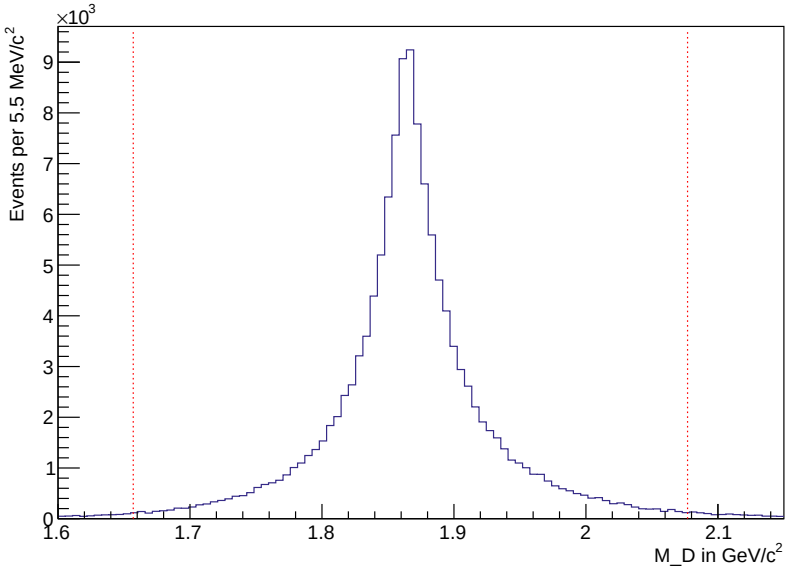

Figure 3.5: distribution in $B^+ \to D\ (K_L\pi\pi)\ \pi^+$ signal MC sample. The red dotted line shows where the selection is applied.

bounded and the bounds are,

$$m_{\pi^+} + m_{\pi^-} \leq m_{\pi\pi} \leq m_D - m_{K_L} \tag{3.12}$$

This $m_{\pi\pi}$ reaches maximum when $\vec{P}_{\pi^+}$ and $\vec{P}_{\pi^-}$ are anti-parallel to each other and $\vec{P}_{K_L} = 0$ and minimum when momentum of pions are parallel to each other with K_L momentum being zero. These points lie on the border of the Dalitz plane. We require that the decay of D meson to satisfy this condition so that points lie inside the Dalitz plane.

3.2.5 Reconstruction of B mesons

The B meson in the decay $B^+ \to DK^+$ ($B^+ \to D\pi^+$) is reconstructed from D meson and a charged kaon (pion) track.

$$P_B = P_D + P_h \tag{3.13}$$

The e^-e^+ B factories provide two kinematic variables that can be used to separate signals from the background and partially reconstructed events. The two kinematic variables are M_{bc} which is a mass-like constraint also known as beam constraint mass and ΔE which is an energy-like constraint whose definitions are,

$$M_{bc} = \sqrt{E_{Beam}^2 - \vec{P}_B^{\,2}} \tag{3.14}$$

$$\Delta E = E_B - E_{Beam} \tag{3.15}$$

where $E_{Beam} = \sqrt{s}/2$, and $\vec{P}_B$ and E_B are the momentum and energy of B candidate in the $\Upsilon(4S)$ frame. A correctly reconstructed B decay will have $\Delta E = 0$ and $M_{bc} = m_B$ where m_B is the nominal mass of B meson (see [47]). Hence, one would observe a peaking distribution peaked at those values. Selection criteria $-0.06 \leq \Delta E \leq 0.06$ GeV is applied to the candidates. The side-band region of ΔE is also included in the selection as it is one of the fit variables and is required in the signal extraction process. The distribution of M_{bc} and ΔE of both signal and generic MC sample is shown in Figure 3.6 & 3.7.

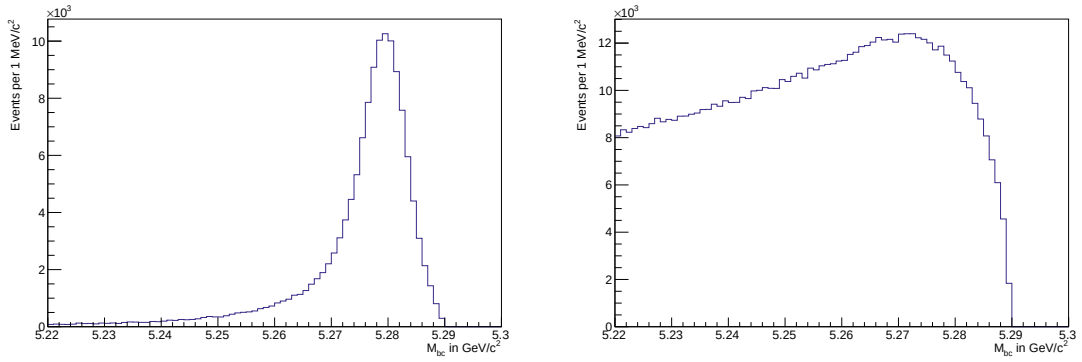

Figure 3.6: M_{bc} distribution of $B^+ \to D\ (K^0_L\pi^+\pi^-)\ K^+$ from signal MC sample (left) and generic MC sample (right). The peak of M_{bc} in signal MC sample is observed at nominal mass of B meson (m_B)

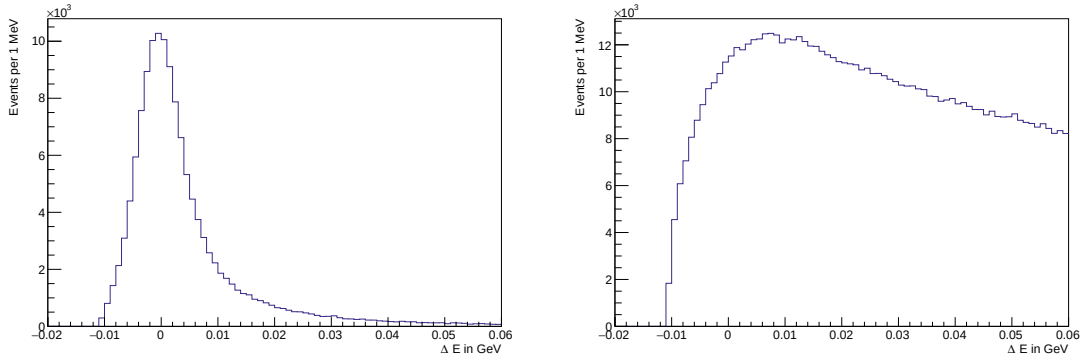

Figure 3.7: ΔE distribution of $B^+ \to D\ (K^0_L\pi^+\pi^-)\ K^+$ from signal MC sample (left) and generic MC sample (right). The peak of ΔE in the signal MC sample is observed around 0

3.3 CONTINUUM BACKGROUND SUPPRESSION

The main background component in the analysis is the continuum event ($e^-\ e^+ \to q\bar{q}$ where $q = u,\ c,\ s,\ d$). The cross-section of continuum events is almost three times the $\Upsilon(4S)$. These events do not contain B meson pair and are more difficult to deal with than any other kind of background as events imitate the signal events. This is problematic because the B mesons reconstructed from these events exhibit a broader distribution in variables such as ΔE and M_{bc} which makes it arduous to isolate the signal events from the dataset.

The suppression of this background can be done by studying the event shape of these two

processes. The two B meson is almost at rest in the center of mass frame. Moreover, their spin-0 nature leads to a uniform distribution of spherical shape for their decay products with no preferred direction. However, the light quarks in the continuum are generated with significantly higher kinetic energy in a back-to-back configuration. Therefore, the produced hadrons exhibit minimal deviation from the quarks' flight direction, giving rise to a jet-like structure, as shown in Fig. 3.8.

The variables that highlight the difference in the event shape between $B\bar{B}$ and the

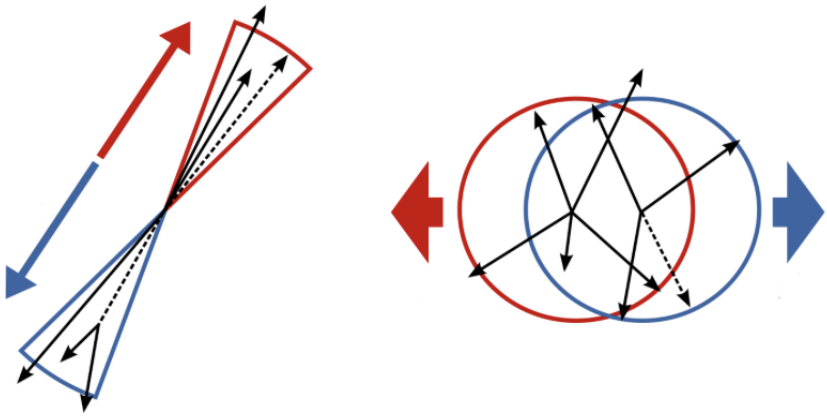

Figure 3.8: Event shape of $e^-e^+ \rightarrow q\bar{q}$ (left) and signal (right). The continuum events are produced in a jet-like shape in contrast to $B\bar{B}$ propagating in a spherical shape. Image is taken from [12]

continuum event are discussed in the next subsection. The B meson for the study of continuum suppression is reconstructed from final state particles which were discussed in detail in the previous section. The remaining final state particles, which are not employed for constructing the B candidate, are utilized to form the rest of the event (ROE) for them. The multivariate analysis (MVA) method [59] called fast boosted decision tree (FBDT) uses a set of input features (variables) to differentiate between a desired event containing $\Upsilon(4S)$ resonance and a continuum event which is discarded based on probability. The BDT is explained in the next subsection.

3.3.1 Boosted decision trees (BDT)

The decision tree internal node divides the variable space into distinct sub-spaces to separate the signal and background. The nodes in a decision tree are determined by a cut value that optimizes the separation between the signal and background classes, resulting in one node with a higher concentration of signal events and the other with more background events. These nodes are then divided into two new child nodes based on whether they meet the cut-off criteria or not. This recursive process continues until every subspace in the feature space contains its own set of signal events. The signal fraction within each node can serve as the output of the classifier. Here, each node represents a threshold value on a specific variable and the leaves (final nodes) represent distinct sub-spaces in variable space. The BDT is shown in Fig 3.9

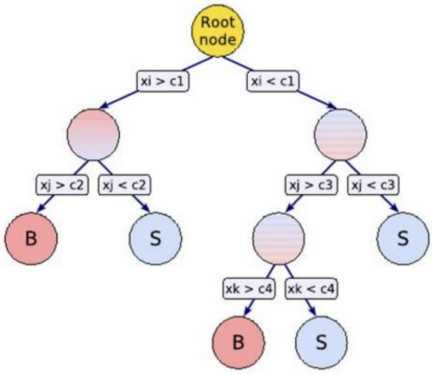

Figure 3.9: Schematic outline of the decision tree. The x_i, x_j and x_k represent cut variables. Taken from [13]

A single decision tree is more prone to over-fitting, which occurs when the model becomes too complex and captures statistical fluctuations in the data rather than the underlying patterns. This can be avoided by reducing the depth of a tree, but it also diminishes the capability to separate background and signal effectively. Such models are called weak learners.

However, many weak learners can be combined to create a strong classifier that is resistant to over-fitting. This is implemented by applying boosting algorithm. The idea behind boosting [60, 61] is to sequentially train a series of weak models, where each subsequent model aims to correct the errors of the previous models. The final model is constructed by combining the predictions of all the weak models, with each model's contribution weighted based on its accuracy on the training data.

BDTs and neural network algorithm (NN) are the most commonly used MVA tool for classification analysis. BDTs are often favoured over NNs due to their robustness and computational efficiency. Their robustness is attributed to their ability to handle outliers and noisy data, while their computational efficiency is due to their ability to train decision trees in parallel. The BDT is already implemented within the basf2 framework. The boosting algorithm that is adopted by Belle II is FastBDT [62] which is also used in this thesis.

3.3.2 Variables to suppress continuum events

The FastBDT takes the following variables as input.

- **Fox-Worlfram moments**[63]: are defined as,

$$H_l = \sum_{i,j} |\mathbf{p_i}||\mathbf{p_j}| P_l(\cos\theta_{ij}) \text{ and } R_l = \frac{H_l}{H_0} \tag{3.16}$$

  where θ_{ij} is the angle between reconstructed momenta of particle i and j $\mathbf{p_i}$ and $\mathbf{p_j}$ in an event and P_l is the l'th order Legendre polynomial. These moments provide information about the shape of the event. A more improved version of the FW moment are the Kakuno-Super-Fox-Wolfram moment (KSFW) [64] which utilises the information of not only the signal B meson but also the opposite (tagging side) B meson and is defined as,

$$H_l^{so} = \sum_{i,j} |\mathbf{p_i}||\mathbf{p_j}| P_l(\cos\theta_{ij}) \tag{3.17}$$

$$H_l^{oo} = \sum_{j,k} |\mathbf{p_j}||\mathbf{p_k}| P_l(\cos\theta_{jk}) \tag{3.18}$$

$$\tag{3.19}$$

where i runs over signal particle and j, k runs over tagging side particle. The moments used as input variables are H_{02}^{so}, H_{10}^{so} and H_{2}^{oo} and R_2 shown in Fig. 3.10 (top left, top right and bottom respectively) which provides better discrimination than other moments.

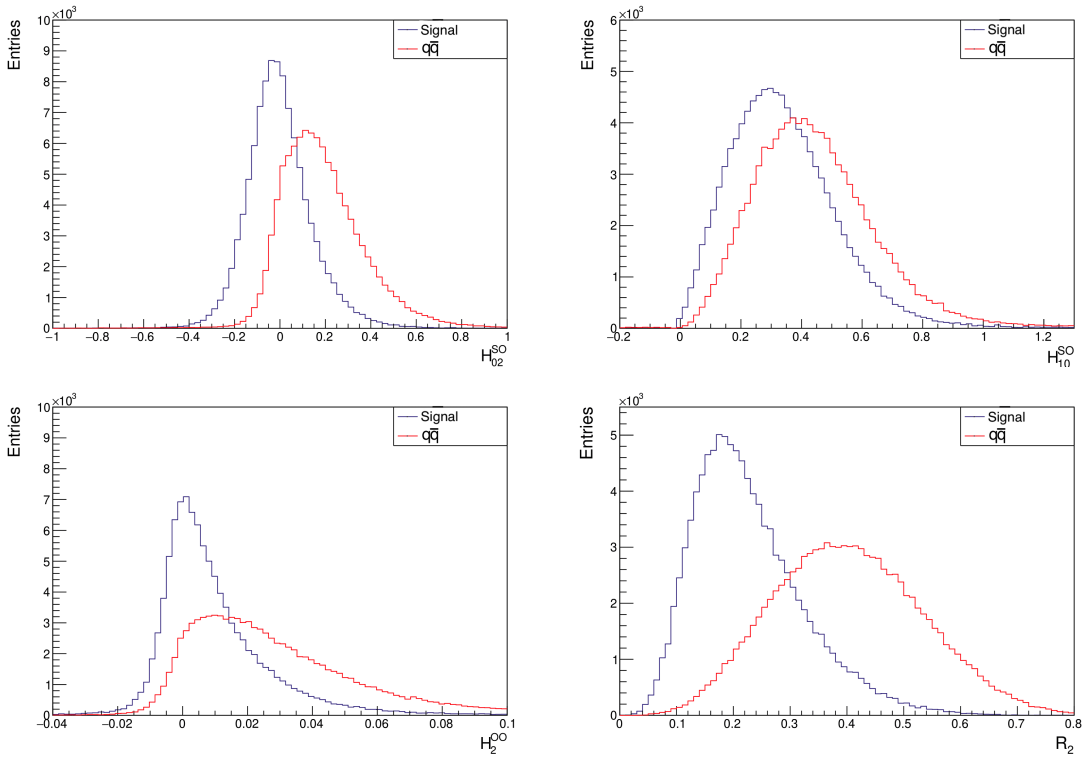

Figure 3.10: Top two plot shows the distribution of input variable H_{02}^{so} and H_{10}^{so}. The bottom plot shows the distribution of H_{2}^{oo}

- **Thrust**: The thrust axis $\vec{T}$ is defined as the unit vector along which the sum of longitudinal momenta of particles is maximum. The magnitude of the thrust axis is given by

$$T = \frac{\sum_i^N |\vec{T} \cdot \vec{p}_i|}{\sum_i^N |\vec{p}_i|} \tag{3.20}$$

  Considering signal particles and those from ROE, two thrust axis can be defined which can be used as discriminating features. Hence, four quantities can be constructed which could give a good measure of discrimination; two magnitudes of thrust axis and two angles they can subtend. One of the input variables used in the analysis is the magnitude of the thrust axis of signal B, denoted by T_{signal} which is shown in Fig. 3.11 (left).

- **Thrust angle**: The cosine of the angle between the signal B thrust axis and thrust axis of ROE is a good variable which differentiates between the event shapes of the signal and continuum events. The B mesons are almost at rest in the CM

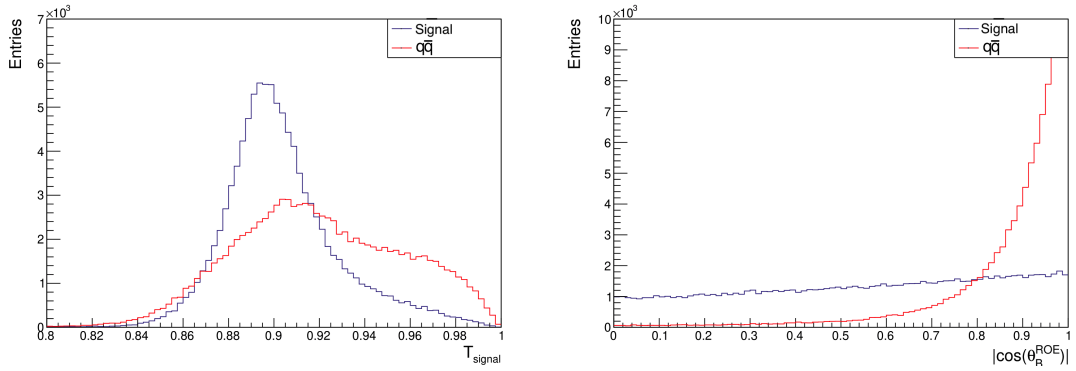

Figure 3.11: The distribution of T_{signal} (left) and $|cos\theta_B^{ROE}|$ variable.

frame of e^-e^+ and are isotropically distributed having a uniform distribution of $|\cos\theta_B^{ROE}|$. However, the continuum events are back to back and have jet-like structures which imply their momentum is directed along a certain direction. As a result, the distribution of $|\cos\theta_B^{ROE}|$ primarily shows a peak at a higher value. The distribution of $|\cos\theta_B^{ROE}|$ is shown in Fig. 3.11 (right).

- **Vertex position**: The boost along the forward direction causes a longer lifetime of B meson than compare to the lighter mesons. As a result, the average distance traversed by B is larger compared to the lighter mesons. Thus the difference in the decay vertex longitudinal component $\Delta z = z_{sig} - z_{tag}$ between B and ROE vertex is an effective feature to discriminate the $B\bar{B}$ events and continuum events. The distribution of Δz is shown in Fig. 3.12 (left).

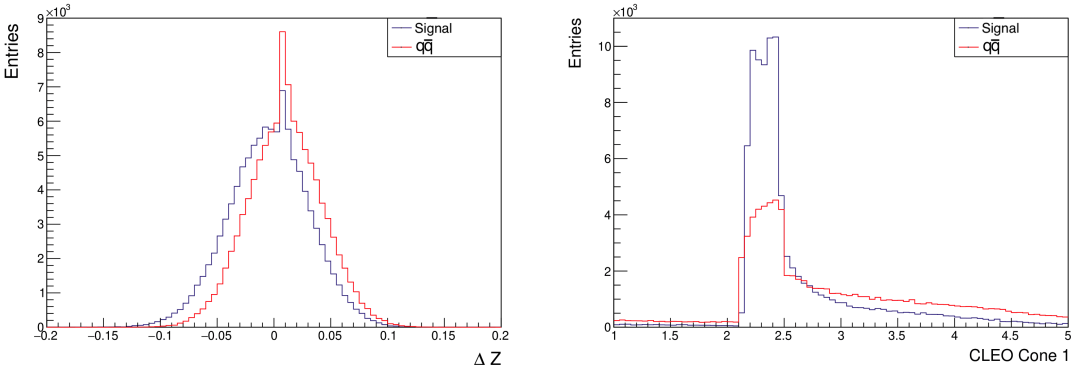

Figure 3.12: The distribution of ΔZ (left) and CLEO Cone 1 (right) is shown.

- **Cleo Cones**: The Cleo Cones were first utilised by CLEO collaboration for the purpose of continuum suppression [65]. For this analysis, space around the candidate thrust axis was divided into 9 cones with 10° of spacing between consecutive cones. These cones measure the scalar momentum flow around the

thrust axis into the cone. Only the first cone distribution is used as an input variable. The distribution of CLEO Cone 1 is shown in Fig. 3.12 (right).

- **Flavour tagging**: The flavour tagger is employed to identify the flavour q of signal B meson. This involves combining various multivariate classifiers into a FastBDT, which takes into account information about the charge of leptons and kaons from the ROE of signal B meson. The algorithm's output is represented by $|q \cdot r|$, where r denotes the quality factor and ranges between 0 (when the algorithm cannot determine the B-tag flavour) and 1 (when the B-tag events are correctly identified). The q takes values ± 1 depending on the flavour of the B meson. The output $|q| = r$ gives the confidence of the prediction. The $|q \cdot r|$ value serves as one of the input variables for the FastBDT which is shown in Fig. 3.13.

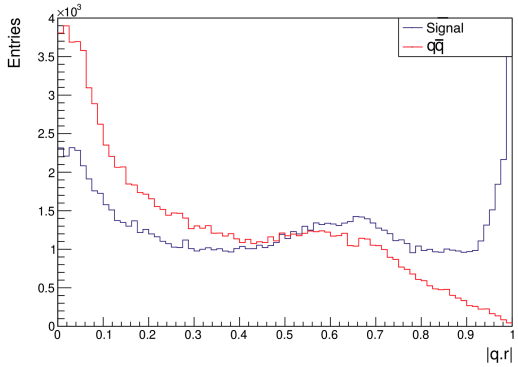

Figure 3.13: The plot shows the distribution of variable $|q \cdot r|$

Importance of variables

The variables are listed in order of their importance (100 - means most important and 0 means least important).

3.3.3 Performance of BDT

In the beginning, the FBDT was trained using many input variables. Subsequently, variables with negligible impact on the performance were removed. The training was performed using 208219 events with 50% of them being signal events from signal MC and 50% of them being continuum events from generic MC.

To validate the performance of the FastBDT, different MC samples of size 56969 events with signal to background ratio being 1:1, were used. The ratio of the MC sample used

Table 3.2: Table of importance of variable

Variable	Importance
$\|cos\theta_B^{ROE}\|$	100
R_2	72
$\|q \cdot r\|$	27
T_{signal}	8
CLEO Cone 1	4
H_{02}^{so}	3
H_{10}^{so}	3
ΔZ	1
H_2^{oo}	0

for testing and training is in the ratio 4 : 1. The performance of the BDT is determined by the ROC (Reciever operating characteristics) curve which portrays the trade-off between the signal efficiency and the background rejection. For an ideally trained FBDT, both signal efficiency and background rejection would be 1. The ROC curve is shown in Fig. 3.14. The area under the curve (AUC) is the metric used to quantify the performance of the ROC curve. The AUC takes a value between 0 and 1 where 0.5 means that it classifies data randomly and 1 means that it is an ideal classifier. The AUC score for both the training set and the testing set is 0.93 in this analysis. We observe that the ROC curve for the train and test sample has the same value of AUC and they coincide which indicates that the model is not over-trained.

The distribution of the classifier output is shown in Figure 3.15. A classifier output of 1 would signify a pure signal, while an output of 0 would signify a pure background. For a perfectly trained model, the training and testing sample must lie within the uncertainties in the over-training plot and the Kolmogorov-Smirnov (KS) test [66] must give a p-value of 1. If the p-value is smaller than 0.05, it shows that the distribution of the predicted probabilities on the training and testing set is significantly different. This may indicate that the model is overfitted and is not able to generalize to new data. The p-value for our analysis is 0.30 for the signal and 0.15 for the background which suggests that the model is not overfitted.

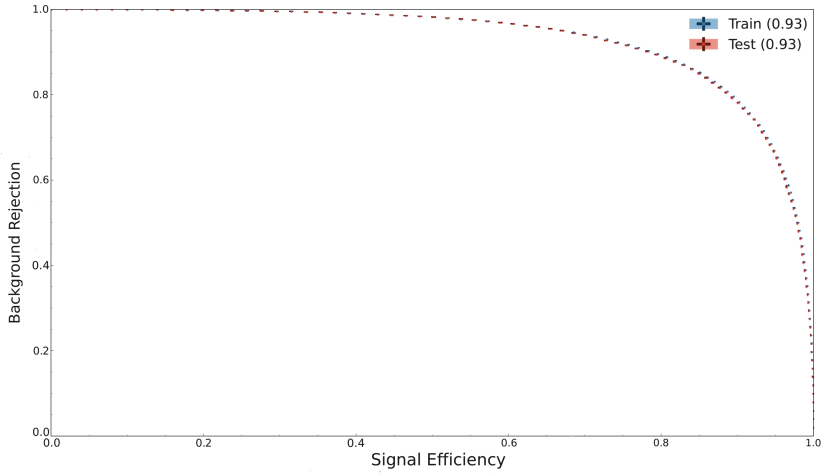

Figure 3.14: ROC plot to assess the performance of the BDT. The vertical axis represents the background rejection rate and the horizontal axis is the signal efficiency. The ROC curve for the training and testing set is shown in blue and red colour respectively.

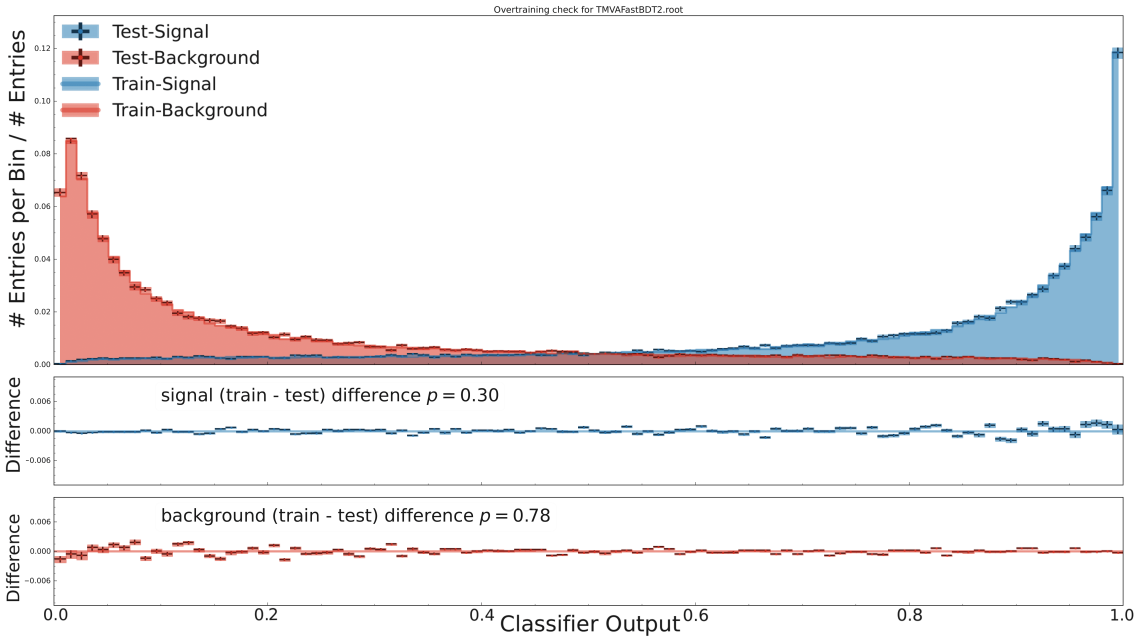

Figure 3.15: The overtraining plot and the distribution of classifier output.

3.3.4 Figure of merit analysis (FOM)

The subsequent step in the analysis is the optimization of the FastBDT to determine the MVA threshold which gives the maximum purity i.e. $\frac{S}{\sqrt{S+B}}$ where S is the number of

signal events and B is the number of background events which includes both continuum ($q\bar{q}$) and combinatorial background ($B\bar{B}$).

The MVA threshold which maximizes the purity of the sample is obtained at 0.93 as

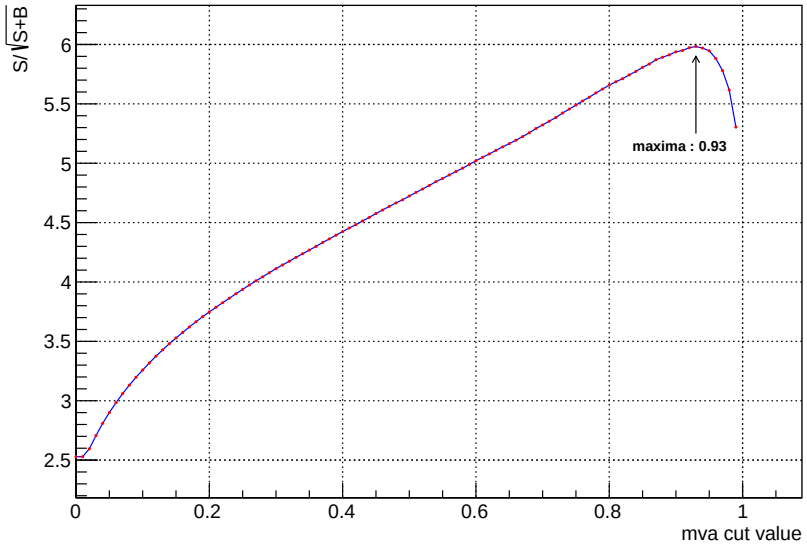

Figure 3.16: The optimization of the MVA cut for the BDT trained on $B \rightarrow D\pi$ channel. The same cut is obtained for $B \rightarrow DK$

can be seen in Figure 3.16. A cut at this threshold rejects 96.66% background with 44% signal efficiency.

3.4 MULTIPLICITY AND BEST CANDIDATE SELECTION

There could be various combinations of the final state particles that satisfy the selection criteria mentioned in previous sections. Because of this, multiple B candidates may emerge from single events. In addition to genuine candidates, randomly misreconstructed tracks can also generate false positives. The distribution of the multiplicity of the candidates after applying all the selection criteria is shown in Fig. 3.17 . The average multiplicity of B candidates obtained is 1.005. A best-candidate selection (BCS) is performed to identify the most optimal candidate from duplicate entries based on some criteria. To identify the optimal candidate in a particular event, the M_{bc} values of all

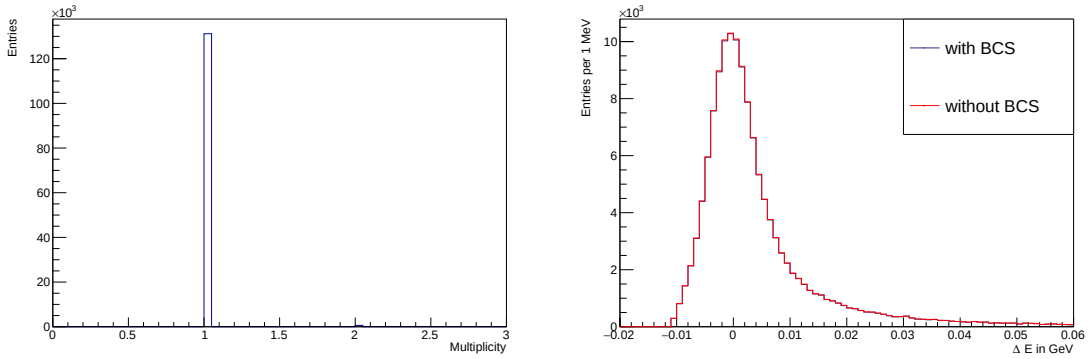

Figure 3.17: The multiplicity of B candidates after applying all the selection criteria on the channel $B^{\pm} \rightarrow DK^{\pm}$ in signal MC. The number of multiple candidates event appears to be very few. The distribution before and after the BCS is shown in the right.

candidates are compared with each other, and the candidate with the M_{bc} value closest to the nominal B mass is chosen.

3.5 IDENTIFICATION OF $B^{\pm} \rightarrow D^{*}h^{\pm}$

The selection criteria that are applied to the data also select the event $B^{\pm} \rightarrow D^{*}h^{\pm}$ along with the signal events. This is problematic because it is very difficult to suppress them. The D^{*} meson decays to a soft photon or soft neutral pions ($D^{*} \rightarrow D\pi^{0}/\gamma$) which have very small momentum and can be absorbed in the kinematic constraint.

The decay branches are identified using the TopoAna tool [67] which is used for topological analysis of the physics processes in Monte Carlo-generated data. This software is capable of accurately identifying and tagging the physics processes within a given dataset and can create a hierarchy of decay processes by correlating the various particles involved. By analyzing the properties of the particles produced in high-energy collisions, the software can reconstruct the decay chains and determine the underlying physical processes that led to their creation. Various analyses are conducted by it, including component analysis, identification of signal decay branches, and different types of selections.

For our analysis, we use TopoAna to identify the decayed branch $B^{\pm} \rightarrow D^{*}h^{\pm}$. It generates a variable which gives the number of such decay branches present in the event. We utilize this variable to extract those events whose topology is,

$$e^{-}\, e^{+} \rightarrow \Upsilon(4S) \rightarrow B^{+}\, B^{-}; \quad B^{\pm} \rightarrow D^{*}h^{\pm} \tag{3.21}$$

The ΔE of $B^{+} \rightarrow D^{*}h^{+}$ distribution is shown in Fig 4.1.

Chapter 4

CONCLUSION AND REMARK

The ϕ_3 has been measured using many multi-body decay of D meson involving K^0_S, $K^\pm$, $\pi^\pm$ and π^0 in the final states. But the involvement of K^0_L has not yet been studied even though it may introduce significantly more events. This thesis has selected a sample of $B^\pm \rightarrow D\,(K^0_L\,\pi^+\,\pi^-)\,h^\pm$ using various selection criteria and FastBDT method. The final result is shown in Fig 4.1.

In the distribution of kaon enhanced sample, $B^+ \rightarrow DK^+$, the peak of the misidentified pion appears to overlap with that of the pure kaon sample. The peak of the pure pion sample also coincides with that of misidentified kaons, but the strength of misidentified kaons is relatively lower. Despite the reduction in the number of signals after applying continuum suppression, there has also been a significant decrease in the background rate. However, the signal remains beneath the large background, reducing our sensitivity to CP violation. While a maximum likelihood fit of ΔE on $B \rightarrow D\pi$ can still be performed, the signal in the $B \rightarrow DK$ mode is currently insufficient for a likelihood to fit to be conducted. The limited number of signal events in the desired decay channel limits the precision of the measurement of the angle ϕ_3 as a result of increasing statistical uncertainties. This is because the statistical uncertainty is proportional to the inverse square root of the number of signal events, so as the number of events decreases, the uncertainty increases. In order to address this, improvements are needed in the efficiency of the KLM detector to select cleaner KLM clusters with better background rejection and in the construction of K^0_L to obtain more K^0_L candidates for analysis. Currently, the simulation of the K^0_L particle in Belle II is not entirely accurate, as the simulated data does not perfectly match the actual data. Therefore, further work is needed to improve the accuracy of the simulation to ensure more reliable results in future analyses.

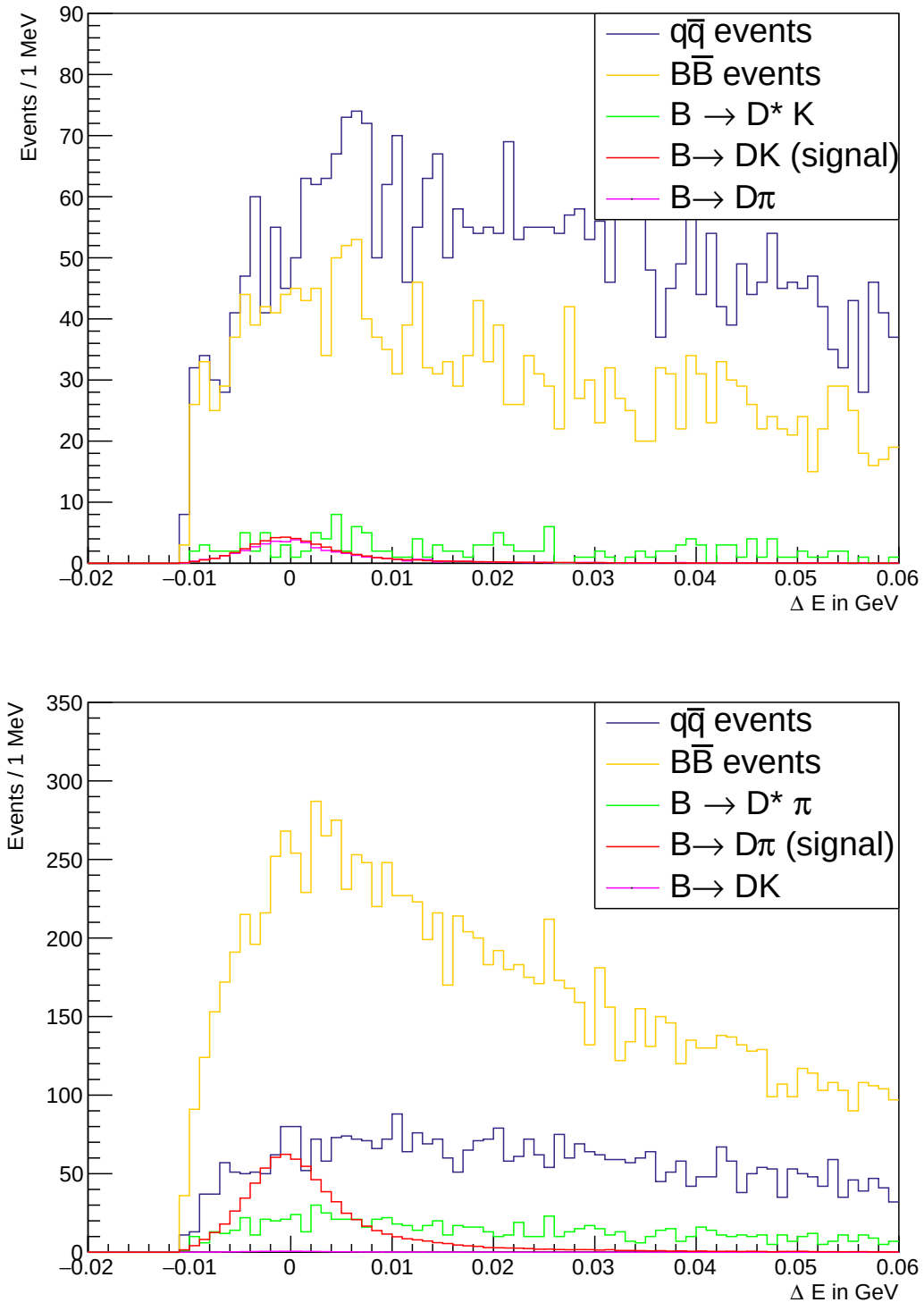

Figure 4.1: The ΔE distribution of different components present in the signal and generic MC. The top plot is for the kaon-enhanced sample $B^+ \to DK^+$ and the bottom plot is for pion enhanced sample $B^+ \to D\pi^+$. The misidentified pions/kaons are represented by magenta.

Appendix A

SIGNAL YIELD DETERMINATION OF $B^+ \to D(K_L\,\pi\,\pi)\pi^+$

This chapter describes the determination of the yield of channel $B^+ \to D(K_L\,\pi\,\pi)\pi^+$ using an unbinned extended maximum-likelihood fit to the prime variable of the analysis (ΔE). Following the selection applied in Chapter 3 to $B^+ \to Dh^+$, we are left with the signal and three distinct background components. The background components are,

- **Continuum Background**: comprising of events coming from $e^-e^+ \to q\bar{q}$ where $q = (u, d, s, c)$.
- **Combinatorial Baclground**: comprising of events arising from misreconstructed candidates $e^-e^+ \to \Upsilon(4S) \to B\bar{B}$.
- **Peaking Background**: comprising of $B^\pm \to Dh^\pm$, $h = \pi$ or K, decays due to the misidentification of $K - \pi$.

The ΔE variable of these components are fitted with different probability distribution function (PDF) separately to extract the yield of the signal and background components. The fit strategy is described in section A.1 and the results of the background, signal and combined fit along with the yield estimate is described in section A.2.

A.1 MAXIMUM LIKELIHOOD FIT

The maximum likelihood (ML) fit is used to estimate the parameter of the probability distribution function (PDF) based on the set of observational data. It involves defining a likelihood function which depends the observed data and the PDF whose parameters are adjusted in such a way that maximizes the value of the likelihood function.

If there are n measurement of variable x and the PDF that describes the data $\{x_i\}_{i=1}^n$ is

$P(x_i, \alpha)$ then the likelihood function $L(x_i, \alpha)$ is defined as

$$L(x_i, \alpha) = \prod_{i=1}^{n} P(x_i, \alpha), \tag{A.1}$$

where α are the unknown parameters whose value is to be determined. The computation becomes simplified when working with the log-likelihood function defined as

$$\ln L(x_i, \alpha) = \sum_{i=1}^{n} \ln P(x_i, \alpha). \tag{A.2}$$

When the data distribution is made up of multiple components that are described by different probability density functions (PDFs), an extended log-likelihood function is used. The unbinned extended log-likelihood function is defined as

$$\mathcal{L}(\alpha) = \sum_{i=1}^{n} \ln \left[\sum_{j=1}^{m} N_j P_j(x_i, \alpha) \right] - \sum_{j=1}^{m} N_j - \ln N!, \tag{A.3}$$

where the index i runs over n measurement and j runs over m different components present in the sample, N_j and P_j are the expected number of event and the PDF of the j^{th} component, respectively, and N is the total number of event in the sample. The parameter α can be estimated by maximizing the extended log-likelihood function:

$$\frac{\mathrm{d}\mathcal{L}(\alpha)}{\mathrm{d}\alpha} = 0. \tag{A.4}$$

By solving the Eq. A.4, the parameters of each component of the PDF can be determined. For this analysis, a pre-loaded ML fitting module called RooFit [68] within the ROOT framework [69] has been utilized. The RooAbsPdf, the base class of RooFit, contains a large number of pre-defined PDFs. Initially, the PDF for the data sample needs to be guessed and defined. Following which, an unbinned extended ML fit is performed on the data sample to estimate the parameter of PDF. The goodness of the fit is described by the quantity χ^2/ndof, where ndof is the number of degrees of freedom. Ideally, when the PDF fits the data perfectly, the value of χ^2/ndof should be equal to 1 and the pull distribution, which represents the distribution of the deviation between the PDF and the data, should be within ± 3 across the entire range of the data.

The probability distribution functions that are used to describe the different components of the data sample used in this analysis are the following,

1. **Crystal Ball**: The crystal ball PDF is defined as

$$f(x;\alpha,n,\mu,\sigma) = N \cdot \begin{cases} e^{-\frac{(x-\mu)^2}{2\sigma^2}} & \text{if } \frac{x-\mu}{\sigma} > -\alpha \\ A \cdot \left(B - \frac{x-\mu}{\sigma}\right)^{-n} & \text{if } \frac{x-\mu}{\sigma} \leq -\alpha \end{cases}, \tag{A.5}$$

   where $A = \left(\frac{n}{|\alpha|}\right)^n e^{-|\alpha|^2/2}$ and $B = \frac{n}{|\alpha|} - |\alpha|$. This definition of crystal ball PDF in RooAbsPdf is implemented within RooCBShape class.

2. **Inverted ARGUS**: The inverted ARGUS is defined as

$$f(x;a,c,p) = N \cdot \begin{cases} (x+a)^p e^{c(1-(x+a)^2)} & \text{if } x > -a \\ 0 & \text{if } x \leq -a \end{cases}. \tag{A.6}$$

   However, this function is not pre-defined within RooAbsPdf but is implemented using the RooGenericPdf module in RooFit.

A.2 FIT RESULTS

An extended maximum likelihood fit is performed on the $B^+ \rightarrow D\pi^+$ samples to estimate the yields. Initially, an individual fit of each component in the sample is carried out. Finally, a combined fit is performed keeping the parameter of individual components fixed to the values obtained from their standalone fits to achieve a reasonable estimate of the statistical precision. The fit results are discussed in the following subsections.

A.2.1 Signal

The RooDataSet module in RooFit was used to generate the unbinned data set for the signal. Subsequently, an appropriate probability distribution function is selected to fit this data. The crystal ball probability distribution function (PDF) is an appropriate fit for describing the distribution of the signal sample. The fit results are shown in Fig. A.1 and the fit parameters obtained are shown in Table A.1.

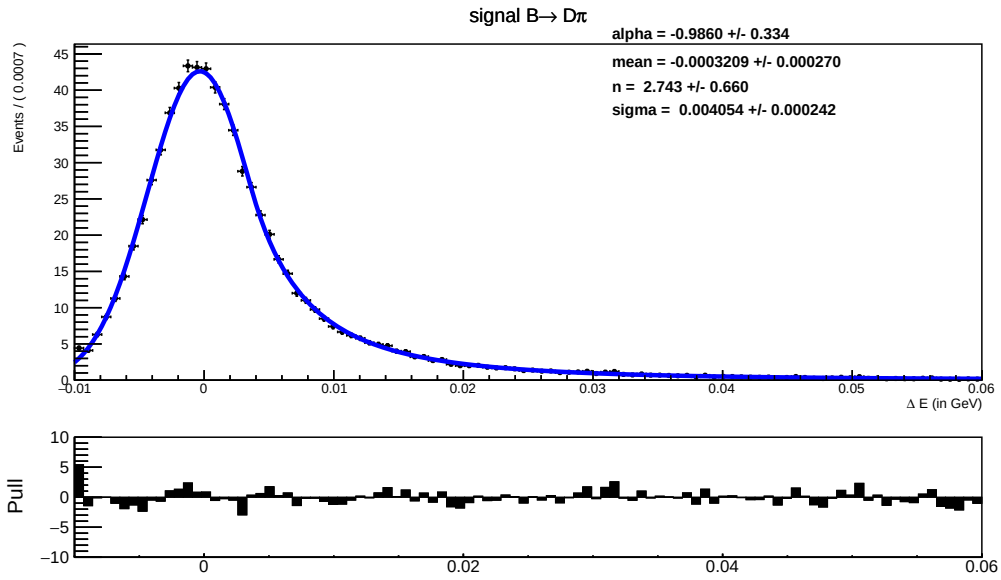

Figure A.1: The ΔE distribution fit of the signal component with the pull distribution. The χ^2/ndof = 1.46 is approximately close to 1 and the pull distribution also is within the ±3 region for the majority of the ΔE range. Thus the crystal ball is a suitable PDF for the above distribution.

Table A.1: Information of the fit parameter of the ΔE distribution of signal component.

Parameter	Fit value
μ	$(-3.210 \pm 2.696) \times 10^{-4}$
σ	$(4.053 \pm 2.423) \times 10^{-4}$
α	$(-9.860 \pm 0.003) \times 10^{-1}$
n	2.743 ± 0.660
χ^2/ndof	1.460

A.2.2 Continuum background

The fitting of the continuum background follows a similar procedure as followed for fitting the signal component. The continuum background consists of events coming from the event $e^-e^+ \rightarrow q\bar{q}$, where $q = u, d, s, c$. The ΔE distribution of the background component must not have a peaking feature as these events arise from off-resonance. Most of these events are rejected after employing an MVA selection and the remaining backgrounds are fitted along with other components. The continuum component can be fitted using an inverted ARGUS PDF. The fit results are shown in Fig. A.2 and the fit

parameters obtained are shown in Table A.2.

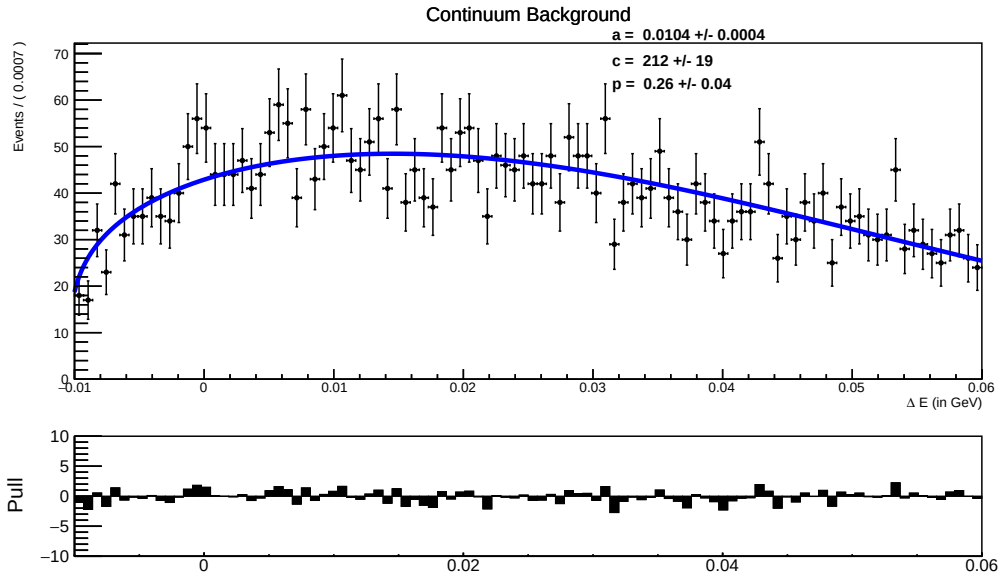

Figure A.2: The ΔE distribution fit of the continuum component with the pull distribution. The χ^2/ndof = 1.10 is approximately close to 1 and the pull distribution is within the ±3 region for most of the ΔE range. Thus the inverted ARGUS is a suitable PDF for the above distribution.

Table A.2: Information of the fit parameter of the ΔE distribution of continuum component.

Parameter	Fit value
a	$(1.041 \pm 0.037) \times 10^{-2}$
p	0.264 ± 0.037
c	211.750 ± 19.174
n	2.888 ± 2.224
χ^2/ndof	1.051

A.2.3 Combinatorial background fit

The fitting of the combinatorial background follows a similar procedure as followed for fitting the signal and continuum component. The combinatorial background consist of the misreconstructed events from $\Upsilon(4S) \rightarrow B^+B^-$ and $\Upsilon(4S) \rightarrow B^0\bar{B}^0$ streams. The ΔE distribution of the background component is fitted with the crystal ball PDF. The fit

results are shown in Fig. A.3 and the fit parameters obtained are shown in Table A.3.

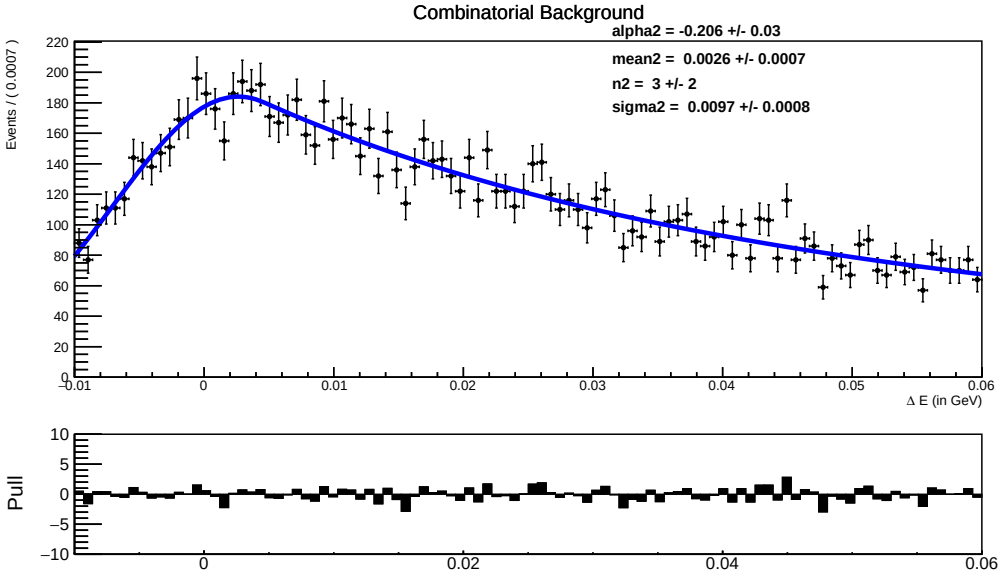

Figure A.3: The ΔE distribution fit of the combinatorial component with the pull distribution. The χ^2/ndof = 1.17 is approximately close to 1 and the pull distribution is within the ±3 region for most of the ΔE range. Thus the crystal ball is a suitable PDF for the above distribution.

Table A.3: Information of the fit parameter of the ΔE distribution of combinatorial component.

Parameter	Fit value
μ	$(2.631 \pm 0.670) \times 10^{-3}$
σ	$(9.744 \pm 0.765) \times 10^{-3}$
α	-0.206 ± 0.034
n	2.888 ± 2.224
χ^2/ndof	1.166

A.2.4 Peaking background

The fitting of the peaking background follows a similar procedure as followed for fitting the other component. The peaking background arises from the misidentification of the K as π in the decay $B^+ \to DK^+$ by the PID detectors (ARICH and TOP). These events are introduced when we apply a pion likelihood selection $\mathcal{L}(\pi/K) < 0.6$. The

background distribution closely resembles that of the signal events $B \rightarrow D\pi$, but the number of events is significantly lower due to the smaller branching fraction of $B \rightarrow DK$ in comparison to $B \rightarrow D\pi$. The ΔE distribution of the background component is fitted with the crystal ball PDF. The fit results are shown in Fig. A.4 and the fit parameters obtained are shown in Table A.4. Since the signal strength is extremely weak compared

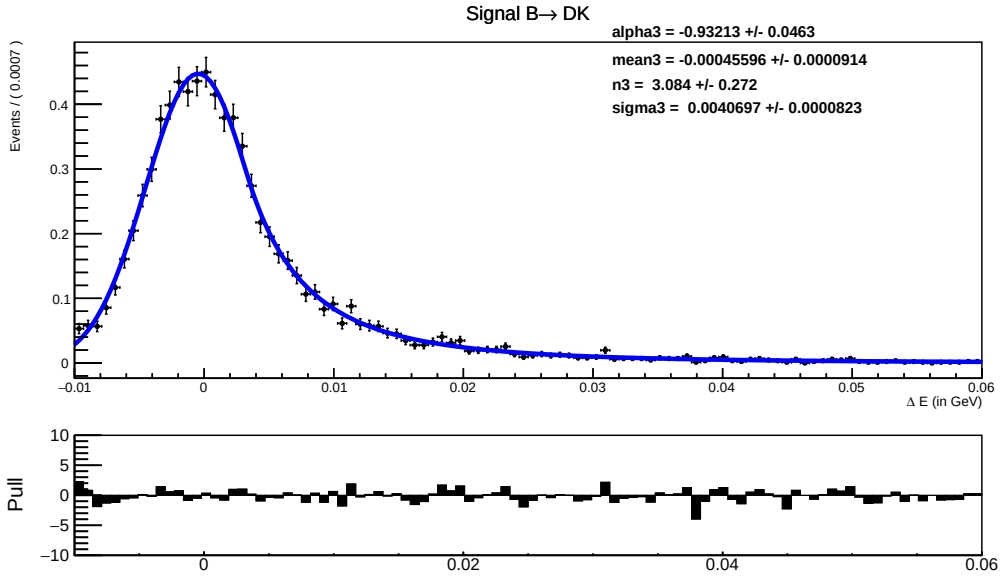

Figure A.4: The ΔE distribution fit of the peaking component with the pull distribution. The χ^2/ndof = 1.10 is approximately close to 1 and the pull distribution is within the ±3 region for most of the ΔE range. Thus the crystal ball is a suitable PDF for the above distribution.

Table A.4: Information of the fit parameter of the ΔE distribution of peaking component.

Parameter	Fit value
μ	$(4.560 \pm 0.914) \times 10^{-4}$
σ	$(4.070 \pm 0.082) \times 10^{-3}$
α	$-0,932 \pm 0.046$
n	3.084 ± 0.272
χ^2/ndof	1.078

to the other components, there will be a significant amount of statistical uncertainty in determining the yield of the peaking background. Therefore, this component will not be taken into account in the combined analysis for this channel.

A.2.5 Combined fit and yield determination

The PDF of the three components, signal, continuum, and combinatorial, are combined using RooAddPdf module of RooFit and a total probability distribution function is obtained which is fitted with the signal and background data sample. The parameters of the total PDF are fixed to the values described in Table A.1, A.2, and A.3. The combined fit result is shown in Fig. A.5. The yield of each of the three components, along with

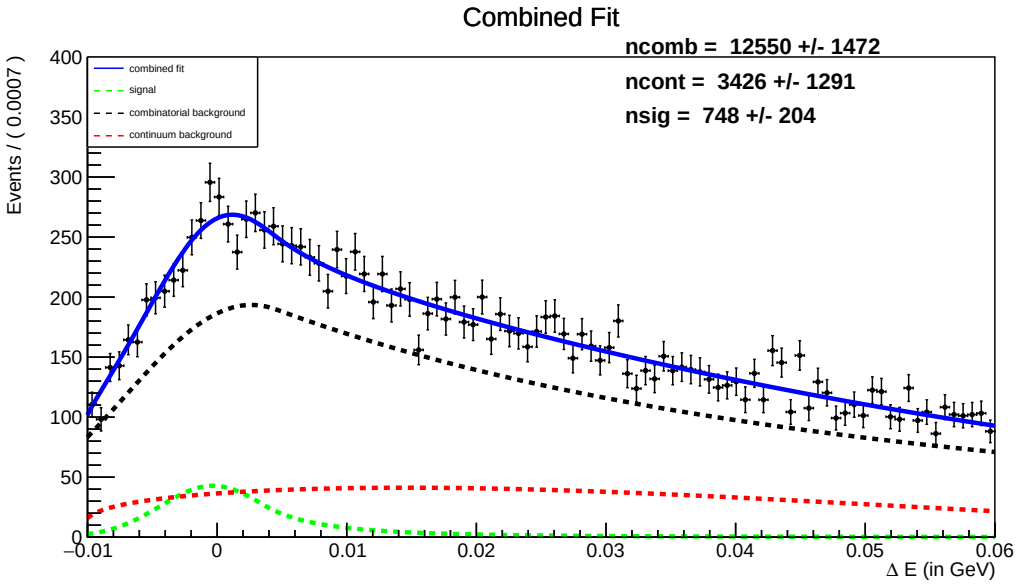

Figure A.5: Final combined fit of the ΔE distribution of $B \rightarrow D\pi$ events. The green dashed curve represents the signal component, the red dashed curve represents the continuum components, the black dashed curve represents the combinatorial component and the blue solid line represents the total PDF.

their corresponding uncertainties, has been determined as follows:

$$N_{sig} = 748 \pm 204 \tag{A.7}$$

$$N_{q\bar{q}} = 3426 \pm 1291 \tag{A.8}$$

$$N_{B\bar{B}} = 12550 \pm 1472 \tag{A.9}$$

The same can be done for the kaon enhanced channel $B^+ \rightarrow DK^+$. However, the extremely low yield of $B^+ \rightarrow D\pi^+$ compared to the background indicates that this channel is not a viable option to proceed further in analysis without a better background

rejection and signal efficiency. This complements the previous analyses performed in this thesis. Moreover, the branching fraction of $B^+ \to DK^+$ is even lower than that of $B^+ \to D\pi^+$, exacerbating the situation. The signal is simply too weak to be distinguished from the background with confidence as low signal yield is associated with large statistical uncertainties. This verifies that the channel $B^\pm \to D(K^0_L\pi^+\pi^-)h^\pm$, $h = K/\pi$ is not feasible enough to perform any CP violation measurement. This marks the end of the analysis with the simulated data.

Bibliography

[1] Wikipedia, "Standard model — Wikipedia, the free encyclopedia," 2023. [Online; accessed 22-April-2023].

[2] M. Tanabashi *et al.*, "Review of Particle Physics," *Phys. Rev. D*, vol. 98, no. 3, p. 030001, 2018.

[3] "Superkekb facility." https://www.ipmu.jp/en/content/de286765-1b4d-4ea5-9c18-22d6942b5a79. Accessed: 2022-04-20.

[4] K. Akai, K. Furukawa, and H. Koiso, "SuperKEKB Collider," *Nucl. Instrum. Meth. A*, vol. 907, pp. 188–199, 2018.

[5] I. Adachi *et al.*, "The belle ii detector," *Nuclear Instruments and Methods in Physics Research Section A*, vol. 907, pp. 46–73, 2018.

[6] L. Zani *et al.*, "The Silicon Vertex Detector of the Belle II experiment," *Nucl. Instrum. Meth. A*, vol. 1038, p. 166952, 2022.

[7] A. Abashian *et al.*, "The belle detector," *Nuclear Instruments and Methods in Physics Research Section A: Accelerators, Spectrometers, Detectors and Associated Equipment*, vol. 479, no. 1, pp. 117–232, 2002.

[8] "Top." https://www2.kek.jp/proffice/archives/feature/2010/BelleIIBPID.html. Accessed: 2022-04-20.

[9] A. Seljak, M. Bračko, R. Dolenec, P. Križan, A. Lozar, R. Pestotnik, and S. Korpar, "LAPPD operation using ToFPETv2 PETSYS ASIC," *JINST*, vol. 18, no. 02, p. C02007, 2023.

[10] T. Abe *et al.*, "Belle II Technical Design Report," 11 2010.

[11] W. Altmannshofer *et al.*, "The Belle II Physics Book," *PTEP*, vol. 2019, no. 12, p. 123C01, 2019. [Erratum: PTEP 2020, 029201 (2020)].

[12] B. I. Collaboration, "Belle ii analysis software framework (basf2) - C++ standard library (stl) containers." https://software.belle2.org/development/sphinx/online_book/basf2/cs.html.

[13] "Decision trees, explained to kids." https://www.science20.com/tommaso_dorigo/decision_trees_explained_to_kids-224948.

[14] Y. Fukuda *et al.*, "Evidence for oscillation of atmospheric neutrinos," *Phys. Rev. Lett.*, vol. 81, pp. 1562–1567, 1998.

[15] Q. R. Ahmad *et al.*, "Direct evidence for neutrino flavor transformation from neutral current interactions in the Sudbury Neutrino Observatory," *Phys. Rev. Lett.*, vol. 89, p. 011301, 2002.

[16] G. Aad *et al.*, "Observation of a new particle in the search for the Standard Model Higgs boson with the ATLAS detector at the LHC," *Phys. Lett. B*, vol. 716, pp. 1–29, 2012.

[17] S. Chatrchyan *et al.*, "Observation of a New Boson at a Mass of 125 GeV with the CMS Experiment at the LHC," *Phys. Lett. B*, vol. 716, pp. 30–61, 2012.

[18] P. Higgs, "Broken symmetries, massless particles and gauge fields," *Physical Review Letters*, vol. 12, pp. 132–133, 1964.

[19] P. Higgs, F. Englert, R. Brout, G. Guralnik, C. Hagen, and T. Kibble, "Broken symmetries and the goldstone theorem," *Physical Review Letters*, vol. 13, pp. 508–511, 1964.

[20] G. Guralnik, C. Hagen, and T. Kibble, "Global conservation laws and massless particles," *Physical Review Letters*, vol. 13, pp. 585–587, 1964.

[21] F. Englert and R. Brout, "Broken symmetry and the mass of gauge vector mesons," *Physical Review Letters*, vol. 13, pp. 321–323, 1964.

[22] E. Noether, "Invariante variationsprobleme," *Göttinger Nachrichten*, vol. 1918, pp. 235–257, 1918.

[23] T. D. Lee and C. N. Yang, "Question of parity conservation in weak interactions," *Physical Review*, vol. 104, pp. 254–258, 1956.

[24] C. S. Wu, E. Ambler, R. W. Hayward, D. D. Hoppes, and R. P. Hudson, "Experimental test of parity conservation in beta decay," *Physical Review Letters*, vol. 105, pp. 1413–1415, 1957.

[25] J. H. Christenson, J. W. Cronin, V. L. Fitch, and R. Turlay, "Evidence for the 2 decay of the k2o meson," *Physical Review Letters*, vol. 13, pp. 138–140, 1964.

[26] R. Aaij and et al., "Observation of cp violation in the b_s^0 meson system," *Physical Letters B*, vol. 712, pp. 203–208, 2012.

[27] B. Aubert and et al., "Observation of cp violation in the b^0 meson system," *Physical Review Letters*, vol. 87, p. 091801, 2001.

[28] K. Abe and et al., "Observation of cp violation in the b^0 meson system," *Physical Review Letters*, vol. 87, p. 091802, 2001.

[29] K. Trabelsi, "Observation of cp violation in the b^0 meson system," *Physical Letters*

B, vol. 712, pp. 203–208, 2012.

[30] R. Aaij and et al., "Measurement of cp violation in $b_s^0 \to d_s^{\mp} k^{\pm}$ decays," *Physical Review Letters*, vol. 122, p. 211803, 2019.

[31] G. Lüders, "On the Equivalence of Invariance under Time Reversal and under Particle-Antiparticle Conjugation for Relativistic Field Theories," *Det Kongelige Danske Videnskabernes Selskab, Matematisk-fysiske Meddelelser*, vol. 28, p. 5, 1954.

[32] A. D. Sakharov, "Violation of cp invariance, c asymmetry, and baryon asymmetry of the universe," *Journal of Experimental and Theoretical Physics Letters*, vol. 5, p. 24, 1966.

[33] N. Cabibbo, "Unitary symmetry and leptonic decays," *Physical Review Letters*, vol. 10, p. 531, 1963.

[34] M. Kobayashi and T. Maskawa, "Cp violation in the renormalizable theory of weak interaction," *Progress of Theoretical Physics*, vol. 49, p. 652, 1973.

[35] P. Zyla *et al.*, "Review of particle physics," *Prog. Theor. Exp. Phys.*, vol. 2020, no. 8, p. 083C01, 2020.

[36] L. Wolfenstein, "Parametrization of the kobayashi-maskawa matrix," *Physical Review Letters*, vol. 51, p. 1945, 1985.

[37] J. E. Augustin, A. M. Boyarski, M. Breidenbach, F. Bulos, J. T. Dakin, G. J. Feldman, G. E. Fischer, D. Fryberger, G. Hanson, B. Jean-Marie, R. R. Larsen, V. Lüth, H. L. Lynch, D. Lyon, C. C. Morehouse, J. M. Paterson, M. L. Perl, B. Richter, P. Rapidis, R. F. Schwitters, W. M. Tanenbaum, F. Vannucci, G. S. Abrams, D. Briggs, W. Chinowsky, C. E. Friedberg, G. Goldhaber, R. J. Hollebeek, J. A. Kadyk, B. Lulu, F. Pierre, G. H. Trilling, J. S. Whitaker, J. Wiss, and J. E. Zipse, "Discovery of a narrow resonance in e^+e^- annihilation," *Phys. Rev. Lett.*, vol. 33, pp. 1406–1408, Dec 1974.

[38] M. Blanke and A. J. Buras, "Flavour physics and cp violation: Present status and future challenges," *Eur. Phys. J. C*, vol. 79, no. 2, p. 159, 2019.

[39] Y. S. Amhis *et al.*, "Averages of b-hadron, c-hadron, and τ-lepton properties as of 2020," *Eur. Phys. J. C*, vol. 81, no. 3, p. 226, 2021.

[40] J. Charles, A. Hocker, H. Lacker, S. Laplace, F. R. Le Diberder, J. Malcles, J. Ocariz, M. Pivk, and L. Roos, "CP violation and the CKM matrix: Assessing the impact of the asymmetric *B* factories," *Eur. Phys. J. C*, vol. 41, no. 1, pp. 1–131, 2005.

[41] J. Brod and J. Zupan, "The ultimate theoretical error on γ from $B \to DK$ decays," *JHEP*, vol. 01, p. 051, 2014.

[42] M. Gronau and D. Wyler, "On determining a weak phase from CP asymmetries in charged B decays," *Phys. Lett. B*, vol. 265, pp. 172–176, 1991.

[43] D. Atwood, I. Dunietz, and A. Soni, "Enhanced CP violation with B —> K D0 (anti-D0) modes and extraction of the CKM angle gamma," *Phys. Rev. Lett.*, vol. 78, pp. 3257–3260, 1997.

[44] D. Atwood, I. Dunietz, and A. Soni, "Improved Methods for Observing CP Violation in $B^{\pm} \to KD$ and Measuring the CKM Phase γ," *Phys. Rev. D*, vol. 63, p. 036005, 2001.

[45] A. Poluektov *et al.*, "Measurement of phi(3) with Dalitz plot analysis of B+- —> D**(*) K+- decay," *Phys. Rev. D*, vol. 70, p. 072003, 2004.

[46] A. Giri, Y. Grossman, A. Soffer, and J. Zupan, "Determining γ using $B^{\pm} \to \mathrm{dk}^{\pm}$ with multibody d decays," *Phys. Rev. D*, vol. 68, p. 054018, Sep 2003.

[47] R. L. Workman *et al.*, "Review of Particle Physics," *PTEP*, vol. 2022, p. 083C01, 2022.

[48] P. del Amo Sanchez *et al.*, "Evidence for direct CP violation in the measurement of the Cabibbo-Kobayashi-Maskawa angle gamma with B-+ —> D(*) K(*)-+ decays," *Phys. Rev. Lett.*, vol. 105, p. 121801, 2010.

[49] A. Poluektov *et al.*, "Evidence for direct CP violation in the decay B->D(*)K, D->KsPi+Pi- and measurement of the CKM phase phi3," *Phys. Rev. D*, vol. 81, p. 112002, 2010.

[50] F. Abudinén *et al.*, "Combined analysis of Belle and Belle II data to determine the CKM angle ϕ_3 using $B^+ \to D(K^0_S h^- h^+)h^+$ decays," *JHEP*, vol. 02, p. 063, 2022. [Erratum: JHEP 12, 034 (2022)].

[51] T. Bilka *et al.*, "Belle II Pixel Detector and Silicon Vertex Detector," in *Proceedings, 10th International Workshop on the CKM Unitarity Triangle*, p. 001, 2020.

[52] M. Staric, K. Inami, P. Krizan, and T. Iijima, "Likelihood analysis of patterns in a time-of-propagation (TOP) counter," *Nucl. Instrum. Meth. A*, vol. 595, pp. 252–255, 2008.

[53] B. Ward, S. Jadach, and Z. Was, "The monte carlo event generator koralw version 1.42 and kkmc version 4.22 for the lepton or quark pair production at lep/slc energies," *Nucl. Phys. B Proc. Suppl.*, vol. 116, pp. 73–80, 2003.

[54] T. Sjöstrand, S. Mrenna, and P. Skands, "Pythia 6.4 physics and manual," *Comput. Phys. Commun.*, vol. 178, no. 11, pp. 852–867, 2008.

[55] D. J. Lange, "The evtgen particle decay simulation package," *Nucl. Instrum. Meth.*

A, vol. 462, no. 1-2, pp. 152–155, 2001.

[56] S. Agostinelli *et al.*, "GEANT4–a simulation toolkit," *Nucl. Instrum. Meth. A*, vol. 506, pp. 250–303, 2003.

[57] P. M. Lewis *et al.*, "First Measurements of Beam Backgrounds at SuperKEKB," *Nucl. Instrum. Meth. A*, vol. 914, pp. 69–144, 2019.

[58] T. Kuhr, C. Pulvermacher, M. Ritter, T. Hauth, and N. Braun, "The Belle II Core Software," *Comput. Softw. Big Sci.*, vol. 3, no. 1, p. 1, 2019.

[59] J. Therhaag, "Tmva toolkit for multivariate data analysis in root," in *Proceedings of the 35th International Conference on High Energy Physics (ICHEP2010)*, p. 510, SISSA Medialab, 2010.

[60] Y. Coadou, "Boosted decision trees and applications," in *EPJ Web of Conferences*, vol. 55, p. 02004, EDP Sciences, 2013.

[61] J. H. Friedman, "Greedy function approximation: A gradient boosting machine," *The Annals of Statistics*, vol. 29, no. 5, pp. 1189–1232, 2001.

[62] T. Keck, "Fastbdt: A speed-optimized and cache-friendly implementation of stochastic gradient-boosted decision trees for multivariate classification," 2016.

[63] G. C. Fox and S. Wolfram, "Observables for the Analysis of Event Shapes in e+ e- Annihilation and Other Processes," *Phys. Rev. Lett.*, vol. 41, p. 1581, 1978.

[64] A. J. Bevan *et al.*, "The Physics of the B Factories," *Eur. Phys. J. C*, vol. 74, p. 3026, 2014.

[65] D. M. Asner *et al.*, "Search for exclusive charmless hadronic B decays," *Phys. Rev. D*, vol. 53, pp. 1039–1050, 1996.

[66] F. J. Massey Jr, "The kolmogorov-smirnov test for goodness of fit," *Journal of the American Statistical Association*, vol. 46, no. 253, pp. 68–78, 1951.

[67] X. Zhou, S. Du, G. Li, and C. Shen, "TopoAna: A generic tool for the event type analysis of inclusive Monte-Carlo samples in high energy physics experiments," *Comput. Phys. Commun.*, vol. 258, p. 107540, 2021.

[68] R. Brun and F. Rademakers, "ROOT: An object oriented data analysis framework," *Nucl. Instrum. Meth. A*, vol. 389, pp. 81–86, 1997.

[69] W. Verkerke and D. Kirkby, "The roofit toolkit for data modeling," 2003.